Document No. 77SDR2314
MSO TR-77-C145

"THE THREE-DIMENSIONAL SHOCK AND PRESSURE (3DSAP) APPROXIMATE FLOW FIELD TECHNIQUE"

Vol. I. Engineering Analysis

General Electric Company
Re-entry and Environmental Systems Division
Philadelphia, Pennsylvania 19101

May 1977

Interim Report for Period November 1976 - May 1977

Work performed under Performance Technology program-G
Contract No: F04701-77-C-0002

Distribution limited to U.S. Government Agencies only (T+E ~~this report contains information applicable to military programs~~), May 1977. Other requests for this document must be referred to Space and Missile Systems Organization, RSSE.

Air Force Space and Missile
Systems Organization
Los Angeles, California

FOREWORD

This report contains the technical work performed for the Performance Technology Program-G, Contract F04701-77-C-0002, Task 2, from November 1976 to May 1977. Bernadette L. Maguire was the Study Program Manager.

When Government drawings, specifications, or other data are used for any purpose other than in connection with a definitely related Government procurement operation, the United States Government thereby incurs no responsibility nor any obligation whatsoever; and the fact that the Government may have formulated, furnished, or in any way supplied the said drawings, specifications, or other data, is not to be regarded by implication or otherwise as in any manner licensing the holder or any other person or corporation, or conveying any rights or permission to manufacture, use, or sell any patented invention that may in any way be related thereto.

This report has been reviewed and is approved.

Robert J. Chambers

R. Chambers, Capt., USAF
Space and Missile Systems Organization (SAMSO)
Air Force Systems Command
Los Angeles, California

Unclassified

SECURITY CLASSIFICATION OF THIS PAGE (When Data Entered)

(18) (19) **REPORT DOCUMENTATION PAGE**

READ INSTRUCTIONS BEFORE COMPLETING FORM

REPORT NUMBER: SAMSO TR-77-C-145-Vol-1	2. GOVT ACCESSION NO. (9) Interim Rept. 11/76 - May 77
4. TITLE (and Subtitle): The Three-Dimensional Shock and Pressure (3DSAP) Approximate Flow Field Technique. Volume I. Engineering Analysis (6)	5. TYPE OF REPORT & PERIOD COVERED: Interim Report: 11/76 to 5/77 on Task 2
	6. PERFORMING ORG. REPORT NUMBER: 77SDR2314-Vol-1 (14)
7. AUTHOR(s): (10) Darryl W. Hall	8. CONTRACT OR GRANT NUMBER(s): (15) F04701-77-C-0002
9. PERFORMING ORGANIZATION NAME AND ADDRESS: General Electric Company, Re-entry and Environmental Systems Division, Philadelphia, Pennsylvania 19101	10. PROGRAM ELEMENT, PROJECT, TASK AREA & WORK UNIT NUMBERS: Task 2
11. CONTROLLING OFFICE NAME AND ADDRESS: Space and Missile Systems Organization (SAMSO), Los Angeles, California (11)	12. REPORT DATE: May 1977 13. NUMBER OF PAGES: 81
14. MONITORING AGENCY NAME & ADDRESS (if different from Controlling Office): Space and Missile Systems Organization (SAMSO), Los Angeles, California (12) 85 p.	15. SECURITY CLASS (of this report): Unclassified 15a. DECLASSIFICATION DOWNGRADING SCHEDULE

16. DISTRIBUTION STATEMENT (of this Report)

Distribution limited to U.S. Government Agencies only (this report contains information not applicable to [redacted]) May 1977. Other requests for this document must be referred to Space and Missile Systems Organization, RSSE. TVE

17. DISTRIBUTION STATEMENT (of the abstract entered in Block 20, if different from Report)

18. SUPPLEMENTARY NOTES

19. KEY WORDS (Continue on reverse side if necessary and identify by block number)

Flow Field
Aerodynamics
Re-entry Vehicles
Asymmetric Nosetips

20. ABSTRACT (Continue on reverse side if necessary and identify by block number)

An approximate flow field technique is developed for the prediction of inviscid aerodynamic characteristics of re-entry vehicles with asymmetric nose geometries at angle of attack and/or sideslip. The subsonic flow region on the nose is approximated using a correlation for surface pressures and iterating on the shock position to satisfy mass continuity. The axisymmetric frustum is computed using the exact three-dimensional inviscid equations, explicitly treating crossflow effects.

DD FORM 1 JAN 73 1473 EDITION OF 1 NOV 65 IS OBSOLETE

Unclassified

SECURITY CLASSIFICATION OF THIS PAGE (When Data Entered)

404 884

TABLE OF CONTENTS

NOMENCLATURE

a	Isentropic speed of sound
A_B	Base area of vehicle, πr_B^2
C_A	Axial force coefficient, $F_A/q_\infty A_B$
C_l	Rolling moment coefficient, $M_Z/q_\infty A_B L$
C_m	Pitching moment coefficient, $M_X/q_\infty A_B L$
C_n	Yawing moment coefficient, $M_Y/q_\infty A_B L$
C_N	Normal force coefficient, $F_N/q_\infty A_B$
C_{N_N}	Nose normal force coefficient, $F_{N_N}/q_\infty \pi r_N^2$
C_p	Pressure coefficient, $(p-p_\infty)/q_\infty$
$C_{p_{MAX}}$	Stagnation point pressure coefficient, $(p_o-p_\infty)/q_\infty$
C_Y	Side force coefficient, $F_y/q_\infty A_B$
D_B	Vehicle base diameter
D_N	Vehicle nose diameter
d_1	Vertical offset of nose cross-section centers
d_2	Lateral offset of nose cross-section centers
e_i	Unit vector in direction of coordinate i
F_A	Axial force
F_N	Normal force
F_{N_N}	Nose normal force
F_Y	Side force
h	Static enthalpy
H	Ratio of local coordinate system curvature to body radius of curvature, $1 + y/R$
H_∞	Total (stagnation) enthalpy, $h + 1/2\,q^2$

K	Curvature of body
L	Vehicle length
L_A	Vehicle length, measured from virtual apex
M	Mach number
M_X	Pitching moment
M_Y	Yawing moment
M_Z	Rolling moment
p	Pressure
P	Logarithm of pressure
q	Total velocity, $\sqrt{u^2+v^2+w^2}$
q_∞	Freestream dynamic pressure, $1/2\,\rho_\infty V_\infty^2$
r	Radial coordinate in cylindrical coordinates
$\hat{r}$	Cross-section radius
r_B	Base radius of vehicle
r_N	Nose radius
R	Body radius of curvature, or gas constant
s	Entropy
T	Temperature
u	Tangential velocity component in body-normal coordinates
v	Normal velocity component in body-normal coordinates
V_∞	Freestream velocity
w	Circumferential velocity component in body-normal coordinates
X, Y, Z	Cartesian coordinates
x	Wetted length, measured along body surface from stagnation point

$X, Y, \bar{Z}$	Location of moment reference point
y	Distance from body surface, measured along body normal
z	Axial coordinate in cylindrical coordinates
z_{cg}	Axial location of moment reference point
α	Angle of attack
β	Sideslip angle
Γ	$\tan^{-1} \beta/\alpha$
γ	Isentropic exponent
ϵ_i	Convergence criteria for iterative calculations
η	Non-dimensional normal coordinate, y/y_s
θ	Circumferential coordinate in (ξ, η, θ) coordinates
θ_b	Local body angle
λ	Characteristic slope
ξ	Wetted length in (ξ, η, θ) coordinates
ρ	Density
σ	Normal streamline slope, v/u
σ_s	Local shock slope, $\tan^{-1} \partial r_s/\partial z$
τ	Circumferential streamline slope, w/u
φ	Circumferential coordinate
$\hat{\varphi}$	Circumferential coordinate (nose geometry)
Ψ	Stream function
$( )_b$	Condition at body
$( )_{EB}$	Equivalent body quantity
$( )_s$	Condition at shock

$( )_o$ Stagnation point condition

$( )_\infty$ Freestream condition

$( )_*$ Sonic point condition

SECTION 1

INTRODUCTION

The determination of the flow environment about a re-entry vehicle is of great importance in both the aerodynamic design and post-flight evaluation efforts. Inviscid flow field solutions may be required in order to define the aerodynamic performance of a vehicle, or as a starting point for making viscous flow and heat transfer analyses.

Aside from expensive and time consuming wind tunnel or flight tests, the standard procedure for the determination of inviscid flow fields about and the associated aerodynamic characteristics of re-entry vehicles is through numerical solution of the inviscid equations of motion. One such numerical technique is the GE Three-Dimensional Flow Field (3DFF) system,[1] which has the capability of obtaining the inviscid flow solution about a wide range of re-entry vehicle geometries. Although far less expensive than wind tunnel tests, exact procedures such as 3DFF may still be too costly for some applications. For example, in the prediction of re-entry vehicle dispersion, it is necessary to evaluate the inviscid aerodynamic environment many times along many trajectories, as pertinent parameters of the problem are varied statistically. Use of an "exact" technique such as 3DFF is not consistent with the formulations required in statistical dispersion codes.

Approximate flow field procedures have been developed in an effort to efficiently provide predictions of surface pressures and shock shapes required in shape change codes and aerodynamic characteristics required for statistical dispersion analyses. In their simplest form, these approximate techniques rely solely on correlations for both pressures and shock shapes.[2] While correlations are probably the most efficient procedures, they tend to be reliable only for the simplest geometries, from which the correlations are derived.

The next degree of sophistication in approximate flow field techniques is to determine the shock position consistent with an assumed surface pressure distribution. With suitable approximations for shock layer distributions of pressure and velocities, such techniques are able to obtain reasonable, consistent approximations to the inviscid flow field at a fraction of the computer time required for detailed inviscid calculations. This approach has been used to develop approximate flow field techniques for axisymmetric

bodies at zero angle of attack, as in Reference (3) for the nose region, and in References (4) and (5).

Because the bulk of the computer time expended in performing exact inviscid calculations is spent in obtaining solutions for the subsonic flow regions, approximate techniques such as described above have the potential of greatly reducing the computer time required for numerical solution of the nosetip flow field. By coupling an approximate transonic procedure to a more exact supersonic afterbody procedure, an efficient, reliable technique for axisymmetric inviscid flow fields may be developed. Two such techniques are the Nose Shape Aerodynamic Routine (NOSAR)[3] and the Shock and Pressure (SAP)[6] routine.

In connection with the evaluation of the roll-trim contribution to the low altitude dispersion of ballistic re-entry vehicles, approximate flow field procedures hold great promise because they allow efficient, repeated calculation of vehicle aerodynamics as a function of nosetip shape along a trajectory. However, efficiency alone is not the only criterion approximate flow field techniques must satisfy; accuracy is also of vital importance. For instance, in the determination of the trim angle of attack due to an asymmetric nose, it is not sufficient to simply obtain an accurate estimate of the nose load; the downstream influence of the ablated nose shape must also be considered. Simple correlations of vehicle surface pressures are not capable of correctly treating this downstream influence, but techniques such as NOSAR and SAP, with direct coupling of the afterbody flow to the approximate solution on the nose, provide accurate results for nearly axisymmetric shapes at small angles of attack using an equivalent body procedure.

The technique developed in this report is an extension to three-dimensions of the SAP technique and is designed to permit evaluation of the aerodynamic characteristics of re-entry vehicles with asymmetric ablated nose shapes. This new technique, the Three-Dimensional Shock and Pressure (3DSAP) routine, is specifically designed for application to the nose-trim problem, where repeated evaluation of the aerodynamics of non-axisymmetric re-entry vehicles is required. Since 3DSAP is a complete flow field technique, it is also capable of providing the inviscid pressure and shock information required for viscous analyses.

3DSAP approximates the nose flow field solution by determining the flow on surfaces

running from the stagnation point to the start of the frustum, neglecting three-dimensional effects. In the transonic portion of the nose, an equivalent axisymmetric body approach is used to determine the shock shape consistent with assumed distributions of surface pressure and profiles of pressure and velocity across the shock layer. This transonic solution technique is a modification of the transonic solution procedure developed for NOSAR.[3] The supersonic portion of each of the nose surfaces is computed using the axisymmetric inviscid equations of motion along the appropriate axisymmetric equivalent body.

On the frustum, 3DSAP integrates the full three-dimensional inviscid equations, explicitly treating crossflow. All 3DSAP calculations may be made using either ideal or equilibrium real gas thermodynamics. Both angle of attack and sideslip can be treated with this procedure.

The 3DSAP procedure described in this report is an extension of the preliminary version of the technique developed as part of the Nose Trim Study,[7] in which a pitch plane of symmetry was assumed. Details on the use of the 3DSAP technique may be found in Volume II of this report.

SECTION 2

ANALYSIS

2.1 Geometric Considerations

The 3DSAP approximate flow field technique has been developed with the goal of providing an efficient aerodynamic prediction capability for ballistic re-entry vehicles with asymmetric ablated nosetips, such as would develop at low altitudes (below 40 KFT). To handle these asymmetric shapes, the procedure for specifying the nosetip geometry must be as general as possible in order to allow definition of any reasonable nosetip shape. On the other hand, frustum ablation is generally small, and it is sufficient to provide only for simple axisymmetric geometries as would be found on ballistic vehicles, such as conic or biconic afterbodies.

In 3DSAP the nose geometry is defined relative to a user-specified locus of cross-section centers, defined by specification of $d_1(z)$ and $d_2(z)$, as illustrated in Figure 1. At each axial station the cross-section is defined by specification of $\hat{r}(\phi)$, allowing definition of completely arbitrary nose geometries. Special options exist for analytically defining $\hat{r}(\phi)$ for the special cases illustrated in Figure 2, in which each cross-section may be circular, elliptic, bi-elliptic, or quad-elliptic. Provision is also made in 3DSAP for automatic definition of spherical nose shapes, freeing the user of having to provide tabulations of body point geometries for this simple, frequently encountered shape.

For arbitrary cross-sections, circumferential interpolations and derivative evaluations are performed using cubic spline approximations. Evaluations of axial derivatives for non-spherical geometries are performed using the parabolic curve fitting procedure developed in Reference (3) and described in Appendix A.

The stagnation point in 3DSAP is defined by the user with the values of d_1 and d_2 at the first axial station; it is required that $\hat{r} = 0$ at this station. For spherical noses, the stagnation point is located analytically.

For the axisymmetric frustum, the geometry is defined by specifying the coordinate of the start of the frustum and the corresponding radius, z_f and r_f, as well as any two of the three parameters z_b, r_b, and θ_1, illustrated in Figure 3. For biconic frusta, any two of the three additional quantities z_i, r_i, and θ_2 must also be specified.

For the numerical computation of fluid flows it is advantageous to select a coordinate system that is closely aligned with the streamlines of the flow. For bodies of

arbitrary shape, such as ablated nosetips on ballistic re-entry vehicles, an appropriate choice of coordinates is the body-normal coordinate system.

The surfaces to be computed in the nose region of 3DSAP are defined as $\hat{\varphi}$ = constant surfaces, which are equivalent to meridional planes (φ = constant) only if the locus of cross-section centers lies along the vehicle axis ($d_1 = d_2 = 0$). The number of nose surfaces required for a calculation depends on the degree of asymmetry of the nose; a sufficient number must be used to adequately model the important geometric details of the nose shape.

In each of the nose surfaces, body points are defined in a (z, r) coordinate system, where

$$r = \hat{r} + d_1 \cos\hat{\phi} + d_2 \sin\hat{\phi} \tag{2.1.1}$$

is the effective body radius at a given axial station in a given $\hat{\varphi}$ surface. The body-normal coordinate system is then defined in terms of the (z, r) points in a $\hat{\varphi}$ surface as if these points were lying in a plane. The local body angle is computed from

$$\theta_b = \tan^{-1}\frac{dr_b}{dz} \tag{2.1.2}$$

and the wetted length from the stagnation point is determined as

$$x(z) = \int_{z_0}^{z} \frac{d\zeta}{\cos\theta_b(\zeta)} \tag{2.1.3}$$

where the stagnation point is located at $z = z_0$. Any point in the shock layer may be described in terms of either (z, r) or (x, y) coordinates (where y is measured in the direction normal to the body) through the relations

$$r(x,y) = r_b(x) + y\cos\theta_b(x) \tag{2.1.4}$$

$$z(x,y) = z_b(x) - y\sin\theta_b(x) \tag{2.1.5}$$

Other required geometric quantities are the body surface curvature

$$K = \frac{d\theta_b}{dx} \tag{2.1.6}$$

and its negative inverse, the body radius of curvature

$$R = -\left(\frac{d\theta_b}{dx}\right)^{-1}. \tag{2.1.7}$$

As discussed in Reference (6), the body-normal coordinate system is strictly valid only for bodies of continuous curvature. However, by approximating the curvature using finite differences of θ_b, the resulting technique has been found to provide an adequate definition of the coordinate system for bodies with discontinuous curvature.

Equivalent body geometries for the nose calculations are defined relative to a new centerline (about which the equivalent body geometry is assumed to be axisymmetric) that is parallel to the freestream velocity vector and passes through the stagnation point. In the governing equations presented in the next section, the r term that appears must be replaced with the equivalent body value, r_{EB}, to be consistent with the equivalent body analysis. This term may be expressed as

$$r_{EB} = (z - z_0)\sin\alpha_{EB} + (r - r_0)\cos\alpha_{EB} \tag{2.1.8}$$

where

$$\alpha_{EB} = -\alpha\cos\hat{\phi} + \beta\sin\hat{\phi}. \tag{2.1.9}$$

For the supersonic frustum calculations, an equivalent body procedure is not required, as the standard three-dimensional equations of motion are integrated.

2.2 Governing Equations

The governing equations for inviscid, isentropic, compressible, steady flow in the body-normal coordinate system on an axisymmetric body are

CONTINUITY

$$(\rho u r^{\delta_1})_x + (\rho v r^{\delta_1})_y + \delta_2(\rho w r) = 0 \tag{2.2.1}$$

MOMENTUM

$$\frac{Du}{Dt} + \frac{1}{\rho H} P_x + \frac{uv}{RH} - \delta_2 \frac{w^2}{r} \sin\theta_b = 0 \qquad (2.2.2)$$

$$\frac{Dv}{Dt} + \frac{1}{\rho} P_y - \frac{u^2}{RH} - \delta_2 \frac{w^2}{r} \cos\theta_b = 0 \qquad (2.2.3)$$

$$\frac{Dw}{Dt} + \frac{1}{\rho r} P_\phi + \frac{w}{r}(u \sin\theta_b + v \cos\theta_b) = 0 \qquad (2.2.4)$$

ENERGY

$$\frac{DS}{Dt} = 0 \qquad (2.2.5)$$

where the substantial derivative is

$$\frac{D}{Dt} = \frac{u}{H}\frac{\partial}{\partial x} + v\frac{\partial}{\partial y} + \delta_2 \frac{w}{r}\frac{\partial}{\partial \phi} .$$

The above formulation of the governing equations is quite general, since

$\delta_1 = 0, \ \delta_2 = 0$	→	two-dimensional flow
$\delta_1 = 1, \ \delta_2 = 0$	→	axisymmetric body at zero angle of attack and zero sideslip
$\delta_1 = 1, \ \delta_2 = 1$	→	axisymmetric body with crossflow

For closure, equations of state are required. For an ideal gas, the explicit thermodynamic relations used are

$$p = \rho R T \qquad (2.2.6)$$

$$h = \frac{\gamma}{\gamma - 1}\frac{p}{\rho} \qquad (2.2.7)$$

$$\frac{s}{R} = \frac{1}{\gamma - 1}(\log p - \gamma \log \rho). \qquad (2.2.8)$$

For real gas thermodynamics, properties are determined by interpolation on tables of equilibrium air thermodynamic properties. In the interpolation procedure two independent variables are required; these may be any one of the pairs (p, s/R), (p,h), or (p,T). Equations (2.2.1)-(2.2.5) are consistent with the dimensional quantities used in the thermodynamic properties routine.

A transformation of the governing equations is made for use in the supersonic calculations. Defining

$$\xi = x$$

$$\eta = y/y_s \ (x, \varphi)$$

$$\theta = \varphi$$

the transformation yields

$$\frac{\partial}{\partial x} = \frac{\partial}{\partial \xi} - \frac{\eta}{y_s}\frac{\partial y_s}{\partial x}\frac{\partial}{\partial \eta} \qquad (2.2.9)$$

$$\frac{\partial}{\partial y} = \frac{1}{y_s}\frac{\partial}{\partial \eta} \qquad (2.2.10)$$

$$\frac{\partial}{\partial \phi} = \frac{\partial}{\partial \theta} - \frac{\eta}{y_s}\frac{\partial y_s}{\partial \phi}\frac{\partial}{\partial \eta}. \qquad (2.2.11)$$

The continuity equation may be recast in terms of the pressure by noting that

$$\frac{Dp}{Dt} = \frac{1}{a^2}\frac{Dp}{Dt}$$

for isentropic flow. In addition, the three momentum equations are combined to form two equations for the streamline slopes, as suggested by Pandolfi,[8] defined as

$$\sigma = \frac{v}{u} \qquad (2.2.12)$$

$$\tau = \frac{w}{u} \qquad (2.2.13)$$

These two streamline slopes, along with the conservation of total enthalpy and the static enthalpy (determined from the pressure and entropy), will define the three flow components.

In final form the governing equations may be written as

CONTINUITY

$$(1-\frac{a^2}{u^2})P_\xi + (A + \frac{a^2}{u^2}\frac{\eta}{y_s}y_{s_x})P_\eta + BP_\theta + \frac{\sigma H}{y_s}\sigma_\eta$$

$$+ \frac{\sigma H}{r}\left[\delta_1(\sin\theta_b + \sigma\cos\theta_b) + \delta_2(\tau_\theta - \frac{\eta}{y_s}y_{s_\theta}\tau_\eta + \tau^2\sin\theta_b)\right] = 0 \qquad (2.2.14)$$

MOMENTUM

$$\sigma_\xi + A\sigma_\eta + B\sigma_\theta - \frac{a^2}{\sigma u^2}\left[\sigma P_\xi - \frac{1}{y_s}(H + \sigma\eta y_{s_x})P_\eta\right] - \frac{1+\sigma^2}{R}$$

$$- B\tau(\cos\theta_b - \sigma\sin\theta_b) = 0 \qquad (2.2.15)$$

$$\tau_\xi + A\tau_\eta + B\tau_\theta - \frac{a^2}{\sigma u^2}\left[\tau P_\xi - \frac{\eta}{y_s}(\tau y_{s_x} - \frac{H}{r}y_{s_\theta})P_\eta - \frac{H}{r}P_\theta\right]$$

$$+ B(\sin\theta_b + \sigma\cos\theta_b) - \frac{\sigma\tau}{R} + B\tau^2\sin\theta_b = 0 \qquad (2.2.16)$$

ENERGY

$$S_\xi + AS_\eta + BS_\theta = 0 \qquad (2.2.17)$$

where

$$P = \log p$$
$$A = \frac{1}{y_s}\left[\sigma H - \eta(y_{s_x} + By_{s_\theta})\right]$$
$$B = \delta_2\frac{\tau H}{r}.$$

The third momentum equation is replaced by the requirement that total enthalpy be conserved for this steady, isentropic flow. The term y_{s_x} appearing in the above equations may be determined from the local shock slope, σ_s, in a given surface from

the relation

$$\eta_{sx} = \left(1 + \frac{y_b}{R}\right) \tan(\sigma - \theta_b) \qquad (2.2.18)$$

2.3 Transonic Calculations - Nose Region

In regions of steady subsonic flow, the inviscid equations of motion are elliptic in character, requiring the specification of boundary conditions (which are unknown a priori) to form a well-posed problem. Integration of the exact equations of motion, either steady or unsteady, to obtain the transonic flow field is far too slow and expensive for an approximate technique. However, by making assumptions regarding the surface pressure distribution and the form of pressure and normal velocity profiles along body-normals, the transonic flow problem can be reduced to a tractable form, allowing efficient solution.

The first step in obtaining an approximate transonic solution is to assign the surface pressures at each point being considered on the nose. Two different correlations are used in 3DSAP, depending on whether a particular body point is upstream or downstream of the sonic point in a given nose surface.

The approximate location of the sonic point is determined from a correlation relating the sonic point body angle, θ_*, to the inverse bluntness of the body.[3] (This sonic point location is also used in the automatic determination of the extent of the transonic region to be computed. The last body-normal to be computed in the transonic region is taken to be defined by the body point that is a pre-set number of points (usually one) downstream of the assumed sonic point, or the most forward point on the nose such that no downstream body angle is greater than 45°. The further downstream of these two points defines the end of the transonic region.)

Upstream of the sonic point, in the subsonic region, the surface pressure is assigned from Love's "Newtonian Deficiency Method",[9] as modified in Reference (3), as

$$\frac{p}{p_0} = p_s - (1 - p_{FD})\left\{\frac{p_s - p_\infty}{1 - p_\infty}\right\} \qquad (2.3.1)$$

where

$$P_s = 1 - 1.08 \sin^2\left(\frac{\pi}{2} - \theta_{sLB}\right)$$

$$P_{FD} = 1 - (1 - P_*)\, e^{-\lambda}$$

$$\lambda = 4\sqrt{\log(x/x_*)}$$

$$P_* = 0.532.$$

The value of the stagnation pressure behind a normal shock for a perfect gas is

$$P_0 = P_\infty \left[\frac{(\gamma+1) M_\infty^2}{2}\right]^{\frac{\gamma}{\gamma-1}} \left[\frac{\gamma+1}{2\gamma M_\infty^2 - (\gamma-1)}\right]^{\frac{1}{\gamma-1}} \qquad (2.3.2)$$

For a real gas, the stagnation pressure must be determined by iteration, since pressure is always one of the independent variables in the thermodynamic properties routine. The stagnation pressure is that pressure which, together with the normal shock entropy, defines the correct value of stagnation enthalpy (which is equal to the freestream total enthalpy).

Beyond the sonic point in the transonic region, the surface pressure is assigned from a matched Newtonian plus Prandtl-Meyer expansion, which has been curve fit as (Reference 3)

$$\frac{P}{P_0} = 1 - 1.46143 \sin^2(\phi + \Delta\theta) + 0.51143 \sin^2(\phi + \Delta\theta) \qquad (2.3.3)$$

where

$$\phi = \frac{\pi}{2} - \theta_{bLE}$$

$$\Delta\theta = \theta_* - \frac{50}{180}\pi.$$

The next step in the transonic procedure is to obtain estimates of the shock stand-off distance and the shock slope distribution around the body. The stand-off distance along the stagnation point normal (which is parallel to the freestream velocity vector) is taken from a correlation of stand-off distance for spheres,

$$y_s = \left[\frac{0.6137}{M_\infty^2 - 1} + 0.13\right] R_o \qquad (2.3.4)$$

where R_o is the stagnation point radius of curvature. The shock slope on each body normal is taken from a correlation for spheres given in Reference (2) as

$$\theta_{sLB} = 0.5234 + 0.3333\theta_{bLB} + 0.2122\theta_{bLB}^2. \qquad (2.3.5)$$

Along a given normal, the shock position y_s is initially taken to be the final value of shock position obtained from the local iteration at the previous normal. Based on this estimate of shock position and the shock slope assigned from Equation (2.3.5), the properties downstream of the shock may be computed using the procedure described in Appendix B. The stream function at the shock is defined as

$$\psi_s = \frac{1}{2}(\rho_\infty u_\infty r_{LB}^2). \qquad (2.3.6)$$

Quantities on the body surface are completely defined by the assigned value of pressure, the known value of entropy (which is the stagnation value, since the stagnation streamline wets the body surface), and the kinematic boundary condition, which requires that v = 0 at the surface.

Across the shock layer, the pressure profile is assumed to take the form

$$p(\psi) = p_b + \left(\frac{\psi}{\psi_s}\right)^2 (p_s - p_b). \qquad (2.3.7)$$

Pressures are assigned at points equally spaced in stream function along the normal (x, ψ are von Mises coordinates, where $d\psi = \rho u r dy - \rho v r H dx$). Values of entropy at these points are known by interpolation on a table of entropies downstream of the previous shock points versus the stream function at these shock points, since entropy is conserved

along streamlines for this isentropic flow.

The distribution of normal velocity along a body normal is assumed to be given by

$$v(\psi) = f_v\left(\frac{\psi}{\psi_s}\right) v(\psi_s) \tag{2.3.8}$$

where the function f_v is defined as follows.

On the stagnation streamline, the pressure distribution is taken to be

$$p(y) = p_s + \left(\frac{y}{y_s}\right)(p_s - p_\infty) \tag{2.3.9}$$

Using this pressure distribution, and the stagnation value of entropy, the static enthalpy may be evaluated at each point along the stagnation streamline. Then from the conservation of total enthalpy, and the absence of tangential velocity, the normal velocity may be expressed as

$$v_o(y) = -\sqrt{2(H_\infty - h)} \tag{2.3.10}$$

The function f_v is then defined as

$$f_v\left(\frac{y}{y_s}\right) = \frac{v_o(y)}{v_o(y_s)} \tag{2.3.11}$$

Along other body normals, $u(\psi)$ may be computed once $p(\psi)$, $s(\psi)$, and $v(\psi)$ are known. Computing $h(\psi)$ from $p(\psi)$ and $s(\psi)$, the conservation of total enthalpy gives

$$u(\psi) = \sqrt{2(H_\infty - h) - v^2} \tag{2.3.12}$$

This completes the specification of the flow variables across a given body normal. The mass flow across this normal however, may not be consistent with the assumed shock location. A new shock position for a given normal may be computed from

$$y_s' = \frac{r_{body}}{\cos\theta_{body}} \left[\sqrt{1 + \frac{2\cos\theta_{body}}{r_{body}^2} \int_0^{y_s} \frac{d\psi}{\rho u}} - 1 \right] \qquad (2.3.13)$$

where $\rho(\psi)$ may be determined from $p(\psi)$ and $s(\psi)$. The assumed shock position, y_s, is consistent and is accepted if mass continuity is satisfied, i.e., if

$$\left| \frac{y_s' - y_s}{y_s' + y_s} \right| < \epsilon_1 \qquad (2.3.14)$$

where ϵ_1 is typically 0.005.

If this convergence criterion is not satisfied, a new estimate of y_s is obtained from

$$y_{s(new)} = y_{s(old)} + \epsilon_2 (y_s' - y_{s(old)}) \qquad (2.3.15)$$

where, because of the convergence properties of this iteration, ϵ_2 is typically taken to be 1.1 in order to accelerate the iterative process. Using this new value of y_s, the procedure starting with Equation (2.3.6) is repeated until Equation (2.3.14) is satisfied.

The above procedure is followed along each normal in the transonic region in turn, starting with the first normal downstream of the stagnation normal, resulting in a shock shape that is consistent with mass continuity for the assumed distribution of shock slopes. (The shock position on the stagnation normal is obtained by parabolic extrapolation from the two adjacent normals.) The transonic procedure in 3DSAP is structured to allow a global iteration on shock slopes, in which the computed shock positions (at the completion of all of the local iterations) are curve fit using the procedure in Appendix A to obtain new estimates of the shock slopes along the body normals. The local iteration procedure along each ray is then repeated to refine the estimates of shock position, using the new shock angles given by

$$\sigma_{s(new)} = \sigma_{s(old)} + \epsilon_3 (\sigma_s' - \sigma_{s(old)}) \qquad (2.3.16)$$

where σ_s' is the new shock angle from the parabolic fit and the damping factor, ϵ_3, is

typically 0.6. The global iteration is assumed to have converged if successive values of shock position (final values of the successive local iterations) satisfy

$$2\left|\frac{y_s - y_{s_L}}{y_s + y_{s_L}}\right| < \epsilon_4 \qquad (2.3.17)$$

where ϵ_4 is typically 0.005.

In practice, the global iteration has been found to be unnecessary for accurate aerodynamic predictions, as will be shown in Section 3. Because of the sensitivity of the convergence of the global iteration to the selection of nose geometry points and to variations of the nose geometry, the standard operating procedure for 3DSAP does not make use of the global iteration.

2.4 Supersonic Calculation - Nose Region and Frustum

Once the tangential velocity component is supersonic at every point along a given body normal, the character of the governing equations changes from elliptic to hyperbolic. Since mixed initial boundary value problems are well-posed for hyperbolic systems, the steady flow equations may then be solved using a forward-marching integration technique.

In terms of the 3DSAP analysis this means that once the approximate transonic solution has been obtained in any given surface on the nose it is then possible to initiate the supersonic equivalent body calculation, which will terminate at the start of the axisymmetric frustum. This procedure is followed in each body surface being computed on the nose. At the completion of the nose supersonic calculations, appropriate initial data for the frustum calculation may be determined by interpolation. The supersonic frustum calculations are performed with four meridional planes, corresponding to the lee, wind, and two side planes; for the case of a pitch plane of symmetry, only three planes are computed on the frustum.

In generating initial data for supersonic calculations in the nose region it is necessary to account for the differing coordinates used in the transonic and supersonic calculations. As developed in Section 2.3, the transonic calculations are performed in von Mises coordinates, where the independent variables are (x, ψ). Along a given body-normal (x = constant) the relationship between ψ and y is expressed as

$$d\psi = \rho u r_{EB}\, dy \qquad (2.4.1)$$

which may be integrated to yield

$$y(\psi) = \frac{r_{b_{LE}}}{\cos\theta_{b_{LE}}}\left[\sqrt{1 + \frac{2\cos\theta_{b_{LE}}}{r_{b_{LE}}^2}\int_0^{\psi}\frac{d\psi}{\rho u}} - 1\right]. \qquad (2.4.2)$$

Knowing the relationship between y and ψ, appropriate values of p, u, v, and ψ for points equally spaced in y along the initial surface can be determined by interpolation. The entropy is determined directly as a function of ψ from the s, ψ table created from the shock points computed in the transonic region. Other thermodynamic properties may be determined in terms of p and s/R for either ideal or real gases.

On the frustum, the planes to be computed are equally spaced in circumferential angle and are selected such that they correspond to lee, wind, and side planes. Defining

$$\Gamma = \tan^{-1}\frac{\beta}{\alpha} \qquad (2.4.3)$$

these four planes (for the general case) correspond to $\varphi = -\Gamma$, $\pi/2 - \Gamma$, $\pi - \Gamma$, and $3\pi/2 - \Gamma$. If a pitch plane of symmetry is present, only three planes are required, corresponding to $\varphi = 0$, $\pi/2$, and π (since β must be zero for a flow field pitch plane of symmetry).

Since the planes to be computed on the frustum do not necessarily correspond to the planes computed on the nose, initial frustum data for p, σ, s, y_s, and y_{s_x} are obtained from the nose surface solutions using cubic spline interpolation. Because crossflow has been neglected in the nose supersonic calculations, it is necessary to generate an initial crossflow slope (τ) distribution for the frustum initial data.

The crossflow at the shock points may be computed directly from the interpolated values of shock position and slopes in the frustum initial surface. At the body, the crossflow is assumed to be zero in the lee ($\varphi = -\Gamma$) and wind ($\varphi = \pi - \Gamma$) planes. In the side planes, the surface crossflow slope is established by simplifying Equation (2.2.16) for conical flow ($\partial/\partial\xi = 0$), resulting in

$$\frac{\tau}{r}\tau_\varphi + \frac{a^2}{\gamma u^2 r}P_\varphi + \frac{\tau}{r}\sin\theta_b\left(1 + \tau^2\right) = 0. \qquad (2.4.4)$$

which may be integrated to yield

$$y(\psi) = \frac{r_{sc}}{\cos\theta_{sc}} \left[\sqrt{1 + \frac{2\cos\theta_{sc}}{r_{sc}^2} \int_0^{\psi} \frac{d\psi}{\rho u}} - 1 \right] . \qquad (2.4.2)$$

Knowing the relationship between y and ψ, appropriate values of p, u, v, and ψ for points equally spaced in y along the initial surface can be determined by interpolation. The entropy is determined directly as a function of ψ from the s, ψ table created from the shock points computed in the transonic region. Other thermodynamic properties may be determined in terms of p and s/R for either ideal or real gases.

On the frustum, the planes to be computed are equally spaced in circumferential angle and are selected such that they correspond to lee, wind, and side planes. Defining

$$\Gamma = \tan^{-1} \frac{\beta}{\delta} \qquad (2.4.3)$$

these four planes (for the general case) correspond to $\varphi = -\Gamma$, $\pi/2 - \Gamma$, $\pi - \Gamma$, and $3\pi/2 - \Gamma$. If a pitch plane of symmetry is present, only three planes are required, corresponding to $\varphi = 0$, $\pi/2$, and π (since δ must be zero for a flow field pitch plane of symmetry).

Since the planes to be computed on the frustum do not necessarily correspond to the planes computed on the nose, initial frustum data for p, c, s, y_s, and y_{s_x} are obtained from the nose surface solutions using cubic spline interpolation. Because crossflow has been neglected in the nose supersonic calculations, it is necessary to generate an initial crossflow slope (τ) distribution for the frustum initial data.

The crossflow at the shock points may be computed directly from the interpolated values of shock position and slopes in the frustum initial surface. At the body, the crossflow is assumed to be zero in the lee ($\varphi = -\Gamma$) and wind ($\varphi = \pi - \Gamma$) planes. In the side planes, the surface crossflow slope is established by simplifying Equation (2.2.16) for conical flow ($\partial/\partial\xi = 0$), resulting in

$$\frac{1}{r}\tau_\varphi + \frac{a^2}{\gamma u^2 r} P_\varphi + \frac{1}{r}\sin\theta_b (1 + \tau^2) = 0. \qquad (2.4.4)$$

Assuming that $|\tau^3| << |\tau|$ and approximating τ_θ and P_θ by finite differences, algebraic relations for τ at the body surface in the side planes result. Values of the crossflow through the shock layer are then determined by linear interpolation between the body and shock values.

At each point in the frustum initial surface the u velocity component is adjusted to be consistent with the interpolated values of σ, τ, P, and s and the known value of H_∞.

The numerical scheme used to integrate the governing equations at field points is the explicit, forward-marching MacCormack scheme,[10] a predictor-corrector method that is of second-order accuracy in the mesh spacing. The brief description of this scheme given here applies to both the three-dimensional frustum calculation and the supersonic calculations on the nose, where, because of the equivalent body procedure used, there is no θ dependence.

Consider a general hyperbolic equation of the form

$$f_\xi + g_\eta + h_\theta = 0. \tag{2.4.5}$$

In the predictor stage of the MacCormack scheme η- and θ- derivatives are approximated as forward differences, as

$$\frac{\partial g_{i,j,k}}{\partial \eta} = \frac{g_{i,j+1,k} - g_{i,j,k}}{\Delta\eta} \tag{2.4.6}$$

and

$$\frac{\partial h_{i,j,k}}{\partial \theta} = \frac{h_{i,j,k+1} - h_{i,j,k}}{\Delta\theta} \tag{2.4.7}$$

where $\xi = \xi_i$, $\eta = j\Delta\eta$, $\theta = k\Delta\theta$. Using these approximations in Equation (2.4.5) the predicted value of f at $\xi = \xi_i + \Delta\xi = \xi_{i+1}$ is calculated from

$$\tilde{f} = f_{i,j,k} + f_\xi \Delta\xi. \tag{2.4.8}$$

In the corrector stage, derivatives are approximated with backward differences using the predicted values of the dependent variables (the $(\tilde{\ })$ data). Thus

$$\frac{\partial \hat{f}}{\partial \eta} = \frac{\tilde{f}_{i,k} - \tilde{f}_{i-1,k}}{\Delta \eta} \tag{2.4.9}$$

$$\frac{\partial \hat{f}}{\partial \theta} = \frac{\tilde{f}_{i,k} - \tilde{f}_{i,k-1}}{\Delta \theta} \tag{2.4.10}$$

Second-order accuracy is achieved by obtaining the corrected value of f at ξ_{i+1} from

$$f_{i+1,j,k} = \frac{1}{2}\left(f_{i,j,k} + \tilde{f}_{i+1,j,k} + \hat{f}_{i+1,j,k}\right). \tag{2.4.11}$$

On the frustum, because of the coarse circumferential spacing used, the standard finite difference procedures described above do not adequately model the circumferential derivatives P_θ and τ_θ. These derivatives may be more accurately approximated by assuming functional forms for $p(\theta)$ and $\tau(\theta)$ at a given axial station and analytically evaluating the derivatives. Assuming cosine variations of pressure in the half-planes $-\Gamma \le \varphi \le \pi - \Gamma$, $\pi - \Gamma \le \varphi \le 2\pi - \Gamma$ (as described in Appendix D), the pressure derivatives may be expressed as

$$P_\theta = 0 \quad , \qquad \phi = -\Gamma, \pi - \Gamma \tag{2.4.12}$$

$$P_\theta = \frac{1}{2p}\left[p(\pi - \Gamma) - p(-\Gamma)\right] \quad , \quad \phi = \frac{\pi}{2} - \Gamma \tag{2.4.13}$$

and

$$P_\theta = \frac{1}{2p}\left[p(-\Gamma) - p(\pi - \Gamma)\right] \quad , \quad \phi = \frac{3\pi}{2} - \Gamma. \tag{2.4.14}$$

Similarly, the crossflow slope τ is assumed to have a sinusoidal variation in each half-plane, with the magnitude of the crossflow being a maximum in each half-plane at $\varphi = \pi/2 - \Gamma$ and $3\pi/2 - \Gamma$. (It is also assumed throughout the frustum calculation that $\tau = 0$ in $\varphi = -\Gamma$ and $\pi - \Gamma$.) The crossflow slope derivatives may then be expressed as

$$\tau_\theta = 0, \qquad \phi = \frac{\pi}{2} - \Gamma, \frac{3\pi}{2} - \Gamma \qquad (2.4.15)$$

$$\tau_\theta = \frac{1}{2}\left[\tau\left(\frac{\pi}{2} - \Gamma\right) - \tau\left(\frac{3\pi}{2} - \Gamma\right)\right], \quad \phi = -\Gamma \qquad (2.4.16)$$

and

$$\tau_\theta = \frac{1}{2}\left[\tau\left(\frac{3\pi}{2} - \Gamma\right) - \tau\left(\frac{\pi}{2} - \Gamma\right)\right], \quad \phi = \pi - \Gamma \qquad (2.4.17)$$

The assumed second order cosine series fit for pressure is a good approximation to the actual circumferential distribution found on axisymmetric frusta at angle of attack. The sinusoidal variation of τ assumed is also a good approximation at small angles of attack, but at higher angles of attack the local maxima of the crossflow magnitude move off the side planes toward the lee plane, and the circumferential distributions of τ are no longer similar to sine curves.

Successful definition of the entropy distribution through the shock layer requires the use of convective differences in both the normal and circumferential directions, as discussed in Reference (1).

The allowable step-size in the MacCormack integration scheme is determined by the Courant-Friedrichs-Lewy[11] (CFL) stability criterion for hyperbolic equations, which simply requires that the numerical domain of dependence must include the entire physical domain of dependence. Because of the large circumferential spacing used in the frustum calculation, limitations on step-size will always be dependent on the spacing of points along body normals. The CFL condition may be expressed as

$$\Delta\xi \leq \frac{y_s \Delta\eta}{\left\{\frac{|u^2\sigma| + a\sqrt{u^2(1+\sigma^2) - a^2}}{u^2 - a^2}\right\}\left\{1 + \eta\frac{y_s}{R}\right\}} \qquad (2.4.18)$$

The allowable $\Delta\xi$ is evaluated at every point at a given ξ station, and the minimum value is taken to be the step-size at that station, to ensure stability at all points.

Application of the MacCormack scheme to Equations (2.2.14)-(2.2.17) yields values of P, σ, τ, and s/R. Values of P and s/R are used as independent variables in determining other thermodynamic properties for either ideal or real gases. Velocity components may be computed from

$$q = \sqrt{2(H_\infty - h)} \qquad (2.4.19)$$

$$u = \frac{\beta}{\sqrt{1+\sigma^2}} \qquad (2.4.20)$$

$$v = \sigma u \qquad (2.4.21)$$

$$w = \tau u \,. \qquad (2.4.22)$$

At body and shock points, where the appropriate boundary conditions are imposed, special procedures are required. For accuracy at these boundary points, which is critical to the success of any flow field calculation, versions of the appropriate characteristic compatibility conditions are integrated in a predictor-corrector sequence. At the body surface, the boundary condition imposed on the flow takes the form $\sigma = 0$ (for the geometries considered in 3DSAP) and hence, $\sigma_\xi = 0$. The derivation of the compatibility condition, which is finally expressed as an equation for P_ξ, may be found in Appendix C.

Aside from the compatibility condition at body points, it is also necessary to have an equation for the convection of entropy and, for frustum calculations, an equation for the circumferential streamline slope, τ. The same equations are used at the body as at field points for these two quantities, s/R and τ. One-sided normal differences are taken at all body points.

The numerical scheme used at body points for the compatibility condition is the Kentzer-Moretti[12] predictor-corrector scheme, in which the compatibility condition is discretized in a manner pioneered by Kentzer[13] and integrated in a scheme consistent with the MacCormack predictor-corrector sequence.

At the shock the boundary conditions take the form of the Rankine-Hugoniot relations across a shock whose position and inclination are unknown a priori. To determine the solution at a shock point an iterative procedure is used in which the shock slope σ_s (and hence, shock location) is varied until the appropriate characteristic compatibility condition, derived in Appendix C, is satisfied. One-sided differences are used

to approximate normal derivatives at shock points. The iterative procedure used is described in Appendix C. This procedure has the advantage of σ_s's being continuous for all geometries, whereas other forms of the shock slope, such as y_{s_x}, are discontinuous at points where the body curvature is discontinuous. Once the shock orientation is known the properties downstream of the shock may be determined using the procedure in Appendix B, completing the specification of data at the shock point.

In the shock calculations on the frustum it is also necessary to know the circumferential variation of shock location. The term $\partial y_s/\partial\phi$ is evaluated at side planes by using a centered difference formula; this term is assumed to be zero in the lee and wind planes.

3DSAP retains the capability developed in Reference (6) for the approximate treatment of small subsonic regions embedded in the supersonic flow field next to the body surface. This capability permits the supersonic flow calculation procedure to continue through small regions in which the steady flow problem is in reality elliptic rather than hyperbolic.

2.5 Calculation of Forces and Moments

Once the surface pressure distribution over the entire vehicle has been determined using the procedures described in the preceding sections, it is possible to calculate the resultant aerodynamic forces and moments on the vehicle. In general, there are three force components and three moments: axial force (F_A), normal force (F_N), side force (F_Y), pitching moment (M_X), yawing moment (M_Y), and rolling moment (M_Z). Sign conventions for these force and moment components are illustrated in Figure 4. All moments are referenced to the moment reference point $(\bar{X}, \bar{Y}, \bar{Z})$.

For a vehicle with a pitch plane of geometric symmetry and zero sideslip, the side force and yawing and rolling moments vanish. In 3DSAP, the vehicle base pressure is always assumed to be p_∞.

The integral expressions for the vehicle forces and moments for both the nose and frustum are presented in Appendix D.

Once the forces and moments have been determined, the associated non-dimensional aerodynamic coefficients are computed from

$$C_A = \frac{F_A}{q_a A_B} \qquad (2.5.1)$$

$$C_N = \frac{F_N}{q_\infty A_B} \tag{2.5.2}$$

$$C_Y = \frac{F_Y}{q_\infty A_B} \tag{2.5.3}$$

$$C_m = \frac{M_X}{q_\infty A_B L} \tag{2.5.4}$$

$$C_n = \frac{M_Y}{q_\infty A_B L} \tag{2.5.5}$$

$$C_\ell = \frac{M_Z}{q_\infty A_B L} \tag{2.5.6}$$

where $q_\infty = 1/2\ \rho_\infty V_\infty^2$, $A_B = \pi r_B^2$, and L is the reference length, measured from the arbitrarily assigned origin of the coordinate system, Z = 0. (Typically, Z = 0 is selected to be either the vehicle stagnation point or virtual apex.) With moments referenced to $Z = \bar{Z}$, the pitch center of pressure location (normalized by the reference length) is defined as

$$\left(\frac{Z_{cp}}{L}\right)_{PITCH} = -\frac{C_m}{C_N} + \frac{\bar{Z}}{L} \tag{2.5.7}$$

and the yaw center of pressure as

$$\left(\frac{Z_{cp}}{L}\right)_{YAW} = -\frac{C_n}{C_Y} \quad \frac{\bar{Z}}{L} \tag{2.5.8}$$

SECTION 3

VALIDATION AND RECOMMENDATIONS FOR USE

In order to assess the accuracy of the 3DSAP approximate flow field technique, comparisons have been made of results obtained with 3DSAP and experimental data for ablated shapes and 3DFF[1] predictions for sphere-cones. These comparisons have been carried out over a wide range of Mach number ($2.5 \leq M_\infty \leq 20$) and angle of attack ($0 \leq \alpha \leq 15°$) in order to assess the range of applicability of the 3DSAP code. The experimental data used for these comparisons was identified and evaluated as part of the Nose Trim Study.[14] (Comparisons of 3DFF predictions to experimental data for the ablated shapes considered may be found in Reference 15.)

Figures 5 and 6 illustrate the ability of 3DSAP to accurately predict sphere-cone aerodynamics (C_N, z_{cp}/L) at Mach numbers of 5 and 20, respectively, compared to 3DFF predictions at angles of attack up to 5° for three different bluntness ratios. Figure 7 shows the corresponding comparisons of inviscid axial force coefficients at these Mach numbers. As is evident from these figures, 3DSAP is capable of closely approximating the 3DFF results.

The real gas capability of 3DSAP is demonstrated in Figure 8, which depicts pitch center of pressure predictions from 3DSAP and 3DFF for a 9° sphere-cone at $M_\infty = 20$ and $\alpha = 1°$ for both ideal and real (60 KFT) gas thermodynamics over a wide range of bluntness ratio. The agreement is seen to be excellent, even in the bluntness range where the center of pressure curve is quite steep.

The ability of 3DSAP to treat a sphere-cone at sideslip is illustrated in Figure 9. (The preliminary version of 3DSAP[7] did not have sideslip capability.) Predictions are compared to 3DFF results for a 9° sphere-cone at $M_\infty = 10$ and $\alpha = 1°$ for $0 \leq \beta \leq 4°$ at three different bluntness ratios. Figure 10 compares 3DSAP and 3DFF predictions of both pitch and yaw centers of pressure for these cases. The accuracy of 3DSAP for sphere-cones at sideslip and angle of attack is comparable to that exhibited at angle of attack alone.

The range of Mach numbers over which 3DSAP produces good results was investigated, as shown in Figure 11. Depicted are 3DSAP predictions for normal force and pitch center of pressure for a 7° cone of 20% bluntness at $\alpha = 1°$ and $2 \leq M_\infty \leq 4$ compared to both 3DFF predictions and ground test data. The 3DSAP calculation at $M_\infty = 2$ failed,

and the deterioration of accuracy in the normal force predictions is evident at $M_\infty = 2.5$; the C_N prediction at $M_\infty = 3$ is 15% low compared to the 3DFF prediction. It thus appears that the lowest Mach number for which 3DSAP produces reasonable results is approximately $M_\infty = 3$. There is no theoretical limit to the highest Mach number that 3DSAP can handle, other than restrictions due to the range of the real gas thermodynamics property tables, which are large enough in extent to include any earth re-entry trajectory.

Figure 12 presents the results of an evaluation of the angle of attack capability of 3DSAP. As evidenced by this figure, results obtained with 3DSAP for a 9° sphere-cone at $M_\infty = 10$ compare favorably with 3DFF predictions up to $\alpha = 10°$. At higher angles of attack, the 3DSAP results deteriorate due to the assumptions made regarding the crossflow distribution, leading to grossly inadequate predictions of frustum surface pressures. Based on these results, the angle of attack range through which 3DSAP results are reliable may be expressed as $\alpha/\theta_c \leq 1$.

3DSAP has exhibited the ability to provide excellent approximations to sphere-cone aerodynamic coefficients over a wide range of freestream Mach number and angle of attack. The ability to predict sphere-cone aerodynamics, however, was not the goal in the development of 3DSAP, which is designed to treat re-entry vehicle configurations with ablated asymmetric nose geometries. As a first step in the validation process for such shapes, comparisons between 3DSAP and ground test data were generated for three symmetric ablated configurations, corresponding to shapes typical of laminar, transitional, and turbulent geometries for ablated carbonaceous nosetips.

Figures 13-15 illustrate the comparisons of 3DSAP predictions to ground test data for a laminar symmetric shape at Mach numbers 5, 10, and 18, respectively. Shown are predictions of normal force, pitching moment, and axial force computed at $\alpha = 1°$; for symmetric shapes at small angles of attack, linear aerodynamics is assumed (constant C_{N_α}, C_{m_α}). It is important to note that accurate predictions of axial force require consideration of viscous effects, which can, in most cases, be safely neglected in the determination of normal force and pitching moment. (Viscous increments to axial force were computed with the General Electric 3-D Viscous code,[16] which is a numerical solution of the integral boundary layer equations.)

The ability of 3DSAP to treat symmetric ablated shapes is further illustrated in Figures 16 and 17. These figures depict the comparison of 3DSAP predictions to

ground test data for transitional (Figure 16) and turbulent (Figure 17) ablated shapes, respectively, at $M_\infty = 5$. As with the laminar shape, the agreement is seen to be excellent.

The final test for the 3DSAP code is to evaluate its behavior for asymmetric ablated shapes. Figures 18 and 19 show comparisons of 3DSAP predictions to ground test data for a laminar asymmetric shape at $M_\infty = 5$; the agreement is seen to be good, but deteriorating at the larger angles of attack due to the approximations made in the treatment of the crossflow on the frustum and neglect of the crossflow on the nose. Using the assumption of linear aerodynamics over the angle of attack range $0° \leq \alpha \leq 2°$, 3DSAP predicts a trim angle for this configuration of 1.47°, and the data indicates a trim angle of 1.20°.

Figures 20 and 21 present a similar comparison for a transitional asymmetric shape at $M_\infty = 5$; the overall agreement is seen to be good. Likewise, Figures 22 and 23 show the same comparisons for the same transitional shape at $M_\infty = 9$.

The final comparison to data for 3DSAP is shown in Figures 24 and 25, comparing predictions to experimental data for a turbulent asymmetric shape at $M_\infty = 5$. Good agreement is evidenced, as with the other cases.

3DSAP has been found to be a reliable technique for the accurate approximation of inviscid aerodynamics of re-entry vehicles with asymmetric nosetips. Because of its efficiency, which will be discussed below, 3DSAP is suitable for applications where computer time required per solution must be minimized. One such application is in statistical dispersion codes, where aerodynamic coefficients must be evaluated repeatedly along trajectories with continuously changing vehicle geometries.

To demonstrate this capability, the postulated shape history shown in Figure 26 was evaluated with the 3DSAP code. (These postulated shapes and the associated trajectory information were obtained from Reference 17.) The results obtained from the 3DSAP code are shown in Figure 27, depicting trim angle of attack and nose normal force predictions along the trajectory. Real gas thermodynamics were used for these calculations, and both circular and bi-elliptic cross-sections for the nose geometry were considered. No major differences were observed between the circular and bi-elliptic cross-section results for these cases.

Also shown in Figure 27 is the trim angle of attack that would be predicted if the trim were assumed to be created solely by the nose normal force, balanced by a restoring moment of a sphere-cone of equivalent bluntness; i.e., α_T is computed from

$$C_{N_N}(z_{cg} - z_{cp_{Nose}}) = \alpha_T (C_{N_\alpha})_{sc} (z_{cp_{sc}} - z_{cg}) \left(\frac{R_B}{R_N}\right)^2$$

Such a determination of trim angle neglects the influence of the asymmetric nose geometry on the frustum pressure distribution; leading to sizeable errors in α_T prediction, as seen in Figure 27. Correct modelling of nose influence on the frustum pressure distribution thus requires a complete flow field technique such as 3DSAP. (The importance of the frustum pressure distribution in the determination of vehicle aerodynamics has also been demonstrated in Reference 15 using 3DFF calculations.)

The application of the 3DSAP approximate flow field technique to the nosetip reconstruction problem is illustrated in the final two figures. Figure 28 depicts several postulated nose shapes for a flight test vehicle, selected such that they agree reasonably well with recession data, as well as having aerodynamic characteristics predicted by 3DFF that agree with those deduced from the vehicle motion data. Each such shape is the result of many 3DFF calculations, in each of which the geometry is varied until a suitable match of aerodynamic characteristics with flight data is obtained.

Figure 29 illustrates the non-rolling trim angle deduced from flight data, compared to α_T predictions obtained from both 3DFF and 3DSAP. Since 3DSAP exhibits good agreement with 3DFF, this approximate technique can greatly reduce the amount of computer time required for a nosetip reconstruction when used for the initial shape selection process. With such an approach, the 3DFF exact flow field technique need be used only for verification of the final shapes selected using 3DSAP predictions of vehicle aerodynamics.

All of the 3DSAP calculations presented above were obtained using the standard operating procedure for 3DSAP, in which no global iteration on shock slopes in the transonic regions is performed. Thus, the shock slopes used for the transonic calculations are simply those assigned from the correlation, Equation (2.3.5). As evidenced by the comparisons to 3DFF predictions and ground test data, this mode of operation is satisfactory for reliable aerodynamic predictions. The use of the global iteration on a regular basis is not recommended, as the calculation of shock slopes based on

shock position can be sensitive to the selection of body point spacing by the user and to sudden variations in the vehicle geometry, and a converged solution cannot be guaranteed.

All of the above calculations were performed using ten points between the body and shock in the supersonic calculations if the freestream Mach number were greater than six ($M_\infty > 6$). At lower Mach numbers, twenty points between body and shock were used to improve resolution of the flow variables across the thicker shock layer. The use of more points across the layer increases the required computer time per calculation, but results in much more accurate aerodynamic predictions at the lower Mach numbers.

3DSAP requires 54,000 (octal) words of storage on the CDC 7600, and run times range from approximately three to fifteen seconds, depending on the configuration under consideration. For example, a typical ideal gas sphere-cone calculation, run out to a bluntness ratio of 0.05, requires 6-8 seconds; a real gas calculation will increase run time by approximately 50%. Sphere-cone calculations with 3DSAP require only 20-30% of the computer time per solution as required by the 3DFF exact flow field technique (which obtains initial data for the afterbody from spherical axisymmetric solutions).

3DSAP calculations on vehicles with asymmetric nose geometries require only 5-10% of the computer time needed by 3DFF per solution. (The increased efficiency of 3DSAP relative to 3DFF for such cases is due to the substantial time saved by 3DSAP in the nose region, where 3DFF requires a three-dimensional time-dependent transonic solution.) For most ablated nose geometries, 3DSAP requires approximately five seconds per solution; in some cases as many as 15 seconds may be required. The cases requiring the longer run times are those where the nosetip has a large region in the supersonic flow regime on the nose where the surface Mach number is only marginally supersonic, necessitating a very small step size for stability of the finite-difference calculation.

SECTION 4

CONCLUSIONS

This report details the analysis of the 3DSAP approximate flow field technique and presents comparisons of 3DSAP predictions to ground test data and exact flow field calculations, demonstrating its capability of providing accurate yet efficient aerodynamic predictions. As a complete flow field procedure, 3DSAP predicts not only vehicle surface pressures and the resulting forces and moments, but also predicts the bow shock shape and shock layer properties. With its coupling of nose and afterbody solutions, 3DSAP inherently treats the influence of the nose flow field on the frustum solution, as required for accurate aerodynamic predictions.

3DSAP has been developed with the goal of providing accurate inviscid aerodynamic predictions, retaining many capabilities found previously only in exact flow field calculations, but requiring only a fraction of the computer time necessary for such techniques. As such, 3DSAP is ideally suited for application to statistical dispersion codes, where vehicle aerodynamics must be evaluated many times along many trajectories to obtain meaningful dispersion statistics. Additionally, because of its accuracy and efficiency, 3DSAP will find application in other aerodynamic evaluation efforts, such as reconstruction of nosetip shapes during re-entry by matching vehicle motion data.

SECTION 5

REFERENCES

1. Kyriss, C. L., and Harris, T. B., "A Three-Dimensional Flow Field Computer Program for Maneuvering and Ballistic Re-entry Vehicles", presented at the 10th U.S. Navy Symposium on Aeroballistics, July 15-17, 1975, Silver Spring, Md., also General Electric TIS 75SDR013, July 1975.

2. Abbett, M. J., and Davis, J. E., "Interim Report Passive Nosetip Technology (PANT) Program, Vol. IV, Heat Transfer and Pressure Distribution on Ablated Shapes, Part II, Data Correlation and Analysis", SAMSO TR-74-86, January 1974.

3. Kyriss, C. L., and Neff, R. S., "An Approximate Flow Field Technique for Ablated Re-entry Configurations (NOSAR)", General Electric TIS 73SD201, January 1973.

4. Abbett, M. J., et al., "Interim Report Passive Nosetip Technology (PANT) Program, Vol. XX., Investigation of Flow Phenomena over Re-entry Vehicle Nosetips", SAMSO TR-74-86, August 1975.

5. Lin, T. C., "Strategic Re-entry Technology Program, Phase IV (STREET-A IV), Final Report, Volume V, Task 4.1.5, Engineering Methods for Steady Flow over Mildly and Severely Indented Nosetips", SAMSO TR-75-269, September 1975.

6. Hall, D. W., "An Approximate Technique for the Calculation of Inviscid Hypersonic Flows", General Electric TIS 75SDR036, December 1975.

7. Hall, D. W., Kyriss, C. L., and Martellucci, A., "Nose Trim Study, Vol. III. An Approximate Three-Dimensional Inviscid Flow Field Technique for Ballistic Re-entry Vehicles with Asymmetric Noses", SAMSO TR-77-46, September 1976.

8. Pandolfi, M., "Numerical Analysis of the Supersonic Flow about Elliptical Cones", Publication No. 157, Istituto di Macchine e Motori per Aeromobili, Torino, February 1974.

9. Love, E. S., Woods, W. C., Rainey, R. W., and Ashby, G. C., Jr., "Some Topics in Hypersonic Body Shaping", AIAA Paper 69-181, January 1969.

10. MacCormack, R. W., "The Effect of Viscosity in Hypervelocity Impact Cratering", AIAA Paper 69-354, 1969.

11. Courant, R., Friedrichs, K., and Lewy, H., "On the Partial Difference Equations of Mathematical Physics", Mathematische Annalen, 100, 32-74, 1928, reprinted in IBM Journal, March 1967.

12. Moretti, G., and Pandolfi, M., "Entropy Layers", Polytechnic Institute of Brooklyn, PIBAL Report 71-33, November 1971.

13. Kentzer, C. P., "Discretization of Boundary Conditions on Moving Discontinuities", presented at the Second International Conference on Numerical Methods in Fluid Dynamics, Berkeley, September 1970.

14. Truncellito, N. T., Komito, E. H., and Martellucci, A., "Nose Trim Study, Vol. I. A Survey and Evaluation of Aerodynamic Ground Test Data on Ablated Nosetip Configurations", GE Doc. No. 76SDR2330, SAMSO TR-77-46, September 1976.

15. Hall, D. W., Kyriss, C. L., Truncellito, N. T., and Martellucci, A., "Nose Trim Study, Vol. II. An Evaluation of the G. E. Three-Dimensional Flow Field Program for Ballistic Re-entry Vehicles with Asymmetric Noses", GE Doc. No. 76SDR2331, SAMSO TR-77-46, September 1976.

16. Hecht, A. M., and Nestler, D., "3-D Viscous Code Development", Final Report, 1975 IR&D Task RPH-14, Technical Memorandum 9154-75-03, General Electric Company, December 1975.

17. Nardo, C., "Minuteman Accuracy Assessment - Asymmetric Shape Change Response", Aerotherm/Acurex Corporation, Mountain View, California, May 1976.

ACKNOWLEDGEMENT

The author wishes to acknowledge the special contributions of C. M. Dougherty for the coding of the 3DSAP technique, and of A. Martellucci, the Aerothermodynamics area leader of the PTP-G effort, and Dr. C. L. Kyriss for their useful advice in the development of this approximate flow field procedure.

APPENDICES

A. PARABOLIC CURVE FIT PROCEDURE

B. SHOCK RELATIONS

C. DERIVATION OF THE CHARACTERISTIC COMPATIBILITY CONDITION

D. FORCE AND MOMENT INTEGRALS

APPENDIX A. PARABOLIC CURVE FIT PROCEDURE

In this section the derivation of the parabolic curve fitting procedure developed in Reference (3) and used in 3DSAP to calculate body slope and curvature and shock slope is presented. Given the body or shock points in the cylindrical (z, r) coordinate system, the radial and axial coordinates are fit as quadratic functions of chord length, thus eliminating difficulties that might otherwise occur as dr/dz approaches infinity.

The procedure used is a 3-point technique; i.e., when determining slope or curvature at a point, the (z, r) locations of the two adjoining points are required. For calculations at a given point, say (z_2, r_2), the adjoining points are then specified as (z_1, r_1) and (z_3, r_3), where $z_1 < z_2 < z_3$.

Let

$$\Delta z_1 = z_2 - z_1$$

$$\Delta z_2 = z_3 - z_2$$

$$\Delta r_1 = r_2 - r_1$$

$$\Delta r_2 = r_3 - r_2$$

$$\ell_1 = \sqrt{(\Delta z_1)^2 + (\Delta r_1)^2}$$

$$\ell_2 = \sqrt{(\Delta z_2)^2 + (\Delta r_2)^2}$$

Fitting the coordinates in chord length l gives

$$z = z_2 + a_z \ell + b_z \ell^2 \tag{A.1}$$

$$r = r_2 + a_r \ell + b_r \ell^2 \tag{A.2}$$

At $l = -l_1$: $z = z_1$ and $r = r_1$, and at $l = l_2$: $z = z_3$ and $r = r_3$. Algebraic manipulation determines the required constants in Equations (A.1) and (A.2) from these conditions to be

$$a_z = \frac{(\Delta z_2)\ell_1^2 + (\Delta z_1)\ell_2^2}{\ell_1 \ell_2 (\ell_1 + \ell_2)} \tag{A.3}$$

$$b_z = \frac{(\Delta z_2)\ell_1 - (\Delta z_1)\ell_2}{\ell_1 \ell_2 (\ell_1 + \ell_2)} \tag{A.4}$$

$$a_r = \frac{(\Delta r_2)\ell_1^2 + (\Delta r_1)\ell_2^2}{\ell_1 \ell_2 (\ell_1 + \ell_2)} \tag{A.5}$$

$$b_r = \frac{(\Delta r_2)\ell_1 - (\Delta r_1)\ell_2}{\ell_1 \ell_2 (\ell_1 + \ell_2)} \tag{A.6}$$

The derivative dr/dz is evaluated from

$$\frac{dr}{dz} = \frac{\frac{dr}{d\ell}}{\frac{dz}{d\ell}} \tag{A.7}$$

where

$$\frac{dz}{d\ell} = a_z + 2b_z \ell \tag{A.8}$$

$$\frac{dr}{d\ell} = a_r + 2b_r \ell . \tag{A.9}$$

The body angle, θ_b, given by

$$\theta_b = \tan^{-1} \frac{dr_b}{dz} \tag{2.1.2}$$

is determined using Equation (A.7) evaluated at (z_2, r_2) where $l = 0$. The same procedure is used to determine the shock slope, σ, in the transonic solution.

The body curvature, $d\theta_b/dx$, is also evaluated using this parabolic fitting procedure for the transonic solution. Differentiation of Equation (2.1.2) (using Equation (A.7) to replace dr/dz) gives

$$\frac{d\theta_b}{dx} = \frac{2}{1 + \left(\frac{dr_b}{dz}\right)^2} \left[\frac{b_r \frac{dz}{d\ell} - b_z \frac{dr}{d\ell}}{\left(\frac{dz}{d\ell}\right)^2 \frac{dz}{d\ell}} \right] \tag{A.10}$$

noting that $d^2r/dl^2 = b_r$, $d^2z/dl^2 = b_z$ at $l = 0$. The term dx/dl is evaluated from

$$\frac{dx}{d\ell} = \sqrt{\left(\frac{dz}{d\ell}\right)^2 + \left(\frac{dr}{d\ell}\right)^2} . \tag{A.11}$$

APPENDIX B. SHOCK RELATIONS FOR REAL AND IDEAL GASES

To determine the properties downstream of a shock wave in a uniform freestream flow, it is necessary to solve the Rankine-Hugoniot conditions:

$$\rho\tilde{u} = \rho_\infty \tilde{u}_\infty \tag{B.1}$$

$$p + \rho u^2 = p_\infty + \rho_\infty u_\infty^2 \tag{B.2}$$

$$h + \tfrac{1}{2}u^2 = h_\infty + \tfrac{1}{2}u_\infty^2 \tag{B.3}$$

where u_∞ is the component of the freestream velocity normal to the shock and $\tilde{u}$ is the downstream normal velocity component.

In the (x, y, φ) coordinate system, the inward normal to the shock is written as

$$\hat{n}_s = e_{n_1}\hat{e}_x + e_{n_2}\hat{e}_y + e_{n_3}\hat{e}_\phi \tag{B.4}$$

where

$$e_{n_1} = \frac{1}{HY} y_{s_x}$$

$$e_{n_2} = -\frac{1}{Y}$$

$$e_{n_3} = \frac{1}{r_s Y} y_{s_\phi}$$

$$Y = \left\{1 + \frac{1}{H^2} y_{s_x}^2 + \frac{1}{r_s^2} y_{s_\phi}^2\right\}^{1/2}$$

The freestream velocity vector may be written as

$$\begin{aligned}\vec{V}_\infty = V_\infty\Big[&\{\sin\theta_b(\sin\beta\sin\phi + \cos\beta\sin\alpha\cos\phi) \\ &+ \cos\theta_b\cos\beta\cos\alpha\big]\hat{e}_x + \{\cos\theta_b(\sin\beta\sin\phi \\ &+ \cos\beta\sin\alpha\cos\phi - \sin\theta_b\cos\beta\cos\alpha\big]\hat{e}_y \\ &+ \{\sin\beta\cos\phi - \cos\beta\sin\alpha\sin\phi\big]\hat{e}_\phi\Big]\end{aligned} \tag{B.5}$$

The velocity component normal to the shock is then

$$\tilde{u}_\infty = V_\infty\Big[\{\cos\beta\cos\alpha\cos\theta_b + \sin\theta_b(\sin\beta\sin\phi + \cos\beta\sin\alpha\cos\phi)\}e_{n_1} + \{-\cos\beta\cos\alpha\sin\theta_b + \cos\theta_b(\sin\beta\sin\phi + \cos\beta\sin\alpha\cos\phi)\}e_{n_2} + \{\sin\beta\cos\phi - \cos\beta\sin\alpha\sin\phi\}e_{n_3}\Big] \tag{B.6}$$

For an ideal gas the Rankine-Hugoniot conditions may be solved explicitly to yield

$$\tilde{u} = \frac{\tilde{u}_\infty(\gamma-1) + 2\gamma/\tilde{u}_\infty}{\gamma+1} \tag{B.7}$$

Once $\tilde{u}$ is known all thermodynamic properties follow from the Rankine-Hugoniot relations and the ideal gas equations of state.

For a real gas, no such simple solution is possible and an iterative technique must be used.

To complete the specification of data on the downstream side of the shock it is necessary to determine the velocity components in the (x,y,φ) system. Since tangential velocity is conserved across a shock, the resulting velocity components may be expressed as

$$u = \vec{V}_\infty \cdot \hat{e}_x - (\tilde{u}_\infty - \tilde{u})e_{n_1} \tag{B.8}$$

$$v = \vec{V}_\infty \cdot \hat{e}_y - (\tilde{u}_\infty - \tilde{u})e_{n_2} \tag{B.9}$$

$$w = \vec{V}_\infty \cdot \hat{e}_\phi - (\tilde{u}_\infty - \tilde{u})e_{n_3} \tag{B.10}$$

It has been found convenient in practice to create a table of shock properties as a function of normal velocity component at the beginning of each 3DSAP computation. Properties for a given shock inclination may then be quickly determined by simple interpolation at every shock point rather than by a time-consuming iteration required in the case of real gas thermodynamics.

APPENDIX C. DERIVATION OF THE CHARACTERISTIC COMPATIBILITY CONDITION

In the theory of partial differential equations a characteristic surface is a surface such that the derivatives of the dependent variables may be indeterminant in the direction normal to the surface. The characteristic compatibility condition is a linear combination of the governing equations valid along this characteristic surface.

For use in 3DSAP, characteristics in the (ξ, η) plane are of interest; any ζ derivatives appearing in the governing equations will be treated as forcing functions. Reducing the three-dimensional problem to two-dimensions results in a characteristic curve, rather than a characteristic surface. The derivation of the characteristic compatibility relation presented here follows that of Rusanov.*

The governing equations of interest may be written as

$$P_\xi + AP_\eta + \frac{\sigma}{u} u_\xi - \frac{\sigma}{u}\frac{\eta}{y_s} y_{sx} u_\eta + \frac{\sigma H}{u y_s} v_\eta = R \tag{C.1}$$

$$u_\xi + Au_\eta + \frac{a^2}{\sigma u^2} P_\xi - \frac{a^2}{\sigma u^2}\frac{\eta}{y_s} y_{sx} P_\eta = R_2 \tag{C.2}$$

$$v_\xi + Av_\eta + \frac{a^2 H}{\sigma u y_s} P_\eta = R_3 \tag{C.3}$$

where

$$A = \frac{1}{y_s}\{\sigma H - \eta(y_{sx} + B y_{s\phi})\}$$

$$R_1 = -\left[\frac{\partial \sigma}{R} + \frac{\sigma H}{r}\delta_1(\sin\theta_b + \sigma\cos\theta_b) + \delta_2\left(BP_\phi + \frac{\sigma H}{ur}\left\{w_\phi - \frac{\eta}{y_s} y_{s\phi} w_\eta\right\}\right)\right]$$

$$R_2 = -\frac{v}{r} + B(w\sin\theta_b - u_\phi)$$

---

*Rusanov, V. V., Journal of Mathematics and Mathematical Physics, 3, 3, 508-527, 1963.

$$R_3 = \frac{u}{R} - B(v_\theta - \omega \cos\Theta_b)$$

$$B = \delta_2 \frac{\tau H}{r}$$

If the characteristic curve is defined as

$$f(\xi,\eta) = 0 \tag{C.4}$$

then the normal to the curve is

$$\vec{N} = \nabla f = (f_\xi, f_\eta). \tag{C.5}$$

The compatibility condition may be expressed as a linear combination of the governing equations where the l_i are the as yet undetermined multipliers. Combining terms, the compatibility condition may then be written as

$$\begin{aligned} &P_\xi\left(l_1 + \frac{a^2}{\delta u} l_2\right) + P_\eta\left(l_1 A - l_2 \frac{a^2}{\delta u} \frac{\eta}{y_s} y_{sx} + l_3 \frac{a^2 H}{\delta u y_s}\right) \\ &+ u_\xi\left(l_1 \frac{\delta}{u} + l_2\right) + u_\eta\left(-l_1 \frac{\delta}{u} \frac{\eta}{y_s} y_{sx} + l_2 A\right) \\ &+ v_\xi(l_3) + v_\eta\left(l_1 \frac{\delta H}{u y_s} + l_3 A\right) = \sum_{i=1}^{3} l_i R_i \end{aligned} \tag{C.6}$$

The terms involving derivatives of P may be viewed as a directional derivative in the direction $\vec{W}_1$, where

$$\vec{W}_1 = \left(l_1 + \frac{a^2}{\delta u} l_2,\ l_1 A - l_2 \frac{a^2}{\delta u} \frac{\eta}{y_s} y_{sx} + l_3 \frac{a^2 H}{\delta u y_s}\right) \tag{C.7}$$

Similarly, derivatives of u and v may also be viewed as directional derivatives in the directions $\vec{W}_2$ and $\vec{W}_3$:

$$\vec{W}_2 = \left(l_1 \frac{\delta}{u} + l_2,\ -l_1 \frac{\delta}{u} \frac{\eta}{y_s} y_{sx} + l_2 A\right) \tag{C.8}$$

$$\vec{W}_3 = \left(l_3,\ l_1 \frac{\delta H}{u y_s} + l_3 A\right) \tag{C.9}$$

For Equation (C.6) to be valid along the characteristic, these directional derivatives must not have any component in the direction of the normal to the characteristic curve (in which direction the derivatives may be indeterminant). This condition may be expressed as

$$\vec{N} \cdot \vec{W}_1 = \vec{N} \cdot \vec{W}_2 = \vec{N} \cdot \vec{W}_3 = 0 \tag{C.10}$$

In matrix form, these equations are

$$\begin{bmatrix} f_\xi + A f_\eta & \frac{a^2}{\partial u}\left(f_\xi - \frac{\eta}{y_s} y_{sx} f_\eta\right) & \frac{a^2 H}{\partial u y_s} \\ \frac{\partial}{u}\left(f_\xi - \frac{\eta}{y_s} y_{sx} f_\eta\right) & f_\xi + A f_\eta & 0 \\ \frac{\partial H}{u y_s} f_\eta & 0 & f_\xi + A f_\eta \end{bmatrix} \begin{Bmatrix} l_1 \\ l_2 \\ l_3 \end{Bmatrix} = 0. \tag{C.11}$$

For a solution to these three homogeneous equations in three unknowns, it is necessary that the determinant of the coefficient matrix vanish. Furthermore, any one of the three unknowns may be scaled arbitrarily. Defining the characteristic slope as

$$\lambda = -\frac{f_\xi}{f_\eta} \tag{C.12}$$

the following quadratic equation results from expansion of the determinant:

$$\lambda^2\left(1 - \frac{a^2}{u^2}\right) - 2\lambda\left(A + \frac{a^2}{u^2}\frac{\eta}{y_s} y_{sx}\right) + A^2 - \frac{a^2}{u^2 y_s^2}\left(H^2 + \eta^2 y_{sx}^2\right) = 0. \tag{C.13}$$

At the body, where $\eta = 0$, $v = 0$, and $H = 1$, this quadratic is readily solved to yield

$$\lambda_{BODY} = -\frac{a}{y_s \sqrt{u^2 - a^2}} \tag{C.14}$$

where the sign in the quadratic formula is chosen such that $\lambda < 0$.

At the shock, where $\lambda > 0$ and $\eta = 1$ the result is

$$\lambda_{shock} = \frac{A + \frac{a'}{u^2 y_s} y_{sx} + \frac{aH}{u y_s} \beta_1}{1 - \frac{a^2}{u^2}} \tag{C.15}$$

where

$$\beta_1 = \left\{ 1 + \sigma^2 - \frac{a^2}{u^2} + \frac{\tau}{r} y_{s\phi} \left(\frac{\tau}{r} y_{s\phi} - 2\sigma \right) \right\}^{1/2}.$$

By choosing the multiplier l_1 to be $\lambda - A$, the system of Equations (C.11) gives the entire set of multipliers to be

$$l_1 = \lambda - A$$
$$l_2 = -\frac{\sigma}{u} \left(\lambda + \frac{\eta}{y_s} y_{sx} \right)$$
$$l_3 = \frac{\sigma H}{u y_s}$$

and the general form of the characteristic compatibility condition is

$$\frac{aH}{u y_s} \beta_1 (P_q + \lambda P_\eta) - \frac{\sigma}{u} \left(A + \frac{\eta}{y_s} y_{sx} \right)(u_q + \lambda u_\eta) + \frac{\sigma H}{u y_s} (v_q + \lambda v_\eta) = \sum_{i=1}^{3} l_i R_i \tag{C.16}$$

BODY POINTS

The inviscid slip boundary condition requires that

$$\vec{q} \cdot \hat{n}_b = 0 \tag{C.17}$$

where the body normal direction is, in general,

$$\hat{n}_b = \frac{-\frac{1}{H} y_{bx} \hat{e}_x + \hat{e}_y - \frac{1}{r_b} y_{b\phi} \hat{e}_\phi}{\left(1 + \frac{1}{H^2} y_{bx}^2 + \frac{1}{r_b^2} y_{b\phi}^2 \right)^{1/2}} \tag{C.18}$$

But since in 3DSAP the body surface is always defined as y = 0, it follows that (C.17) simplifies to v = 0, which in turn gives A = 0. With this result and noting that H = 1 when $\eta = 0$, as at the body, the characteristic compatibility condition at the body may be written as

$$P_\xi = -\lambda P_\eta - \left[BP_\theta + \gamma \left\{ \frac{\sigma_\eta}{y_s} + \frac{1}{r}(\delta_\xi \tau_\theta + \delta_\xi \sin\theta_s) + \tau B_\xi \left(\theta_\xi - \frac{\cos\theta_s}{y_s \lambda} \right) - \frac{1}{\lambda y_s R} \right\} \right] \Big/ \left(1 - \frac{a^2}{u^2}\right). \qquad \text{(C.19)}$$

This equation replaces the continuity equation in the computational procedure used at body points, as described in Section 2.4, and is integrated in a predictor-corrector sequence.

SHOCK POINTS

The form of the characteristic compatibility condition that applies at the shock is simply that of Equation (C.16), with $\eta = 1$ and λ's being given by Equation (C.15). This equation is the only condition required at the shock; once the shock position and slopes are known the properties downstream of the shock may be obtained from the Rankine-Hugoniot conditions.

Equation (C.16) is solved iteratively, by finding a value of σ ($= \tan^{-1} \partial r_s / \partial z$) for which the compatibility condition is satisfied. ξ - derivatives are approximated by simple two-point differences between the shock properties at the previous step and those that result from the current guess on σ in the iteration.

A predictor-corrector scheme has been devised for this iterative process to make it compatible with the predictor-corrector sequence used at field and body points. In the predictor stage, the coefficients and η - derivatives in Equation (C.16) are evaluated at the last station computed and predicted values of shock location, slope and downstream properties are obtained. In the corrector stage, the coefficients and η - derivatives are taken to be averages of their values at the last station and from the predictor stage.

The iteration on σ is considered to be converged when the difference between the left- and right-hand sides of Equation (C.16) is sufficiently small. An alternate convergence criterion is also used in this iterative process, in which convergence is assumed when successive values of σ in the iteration are essentially unchanged.

This iterative approach has been selected for use in the shock point calculations

because of difficulties encountered in using analytical approaches (e.g., the Kentzer-Moretti scheme) with the body-normal coordinate system in regions where the body curvature is not well-behaved. In such regions, such as might occur in the supersonic regions of ablated nose shapes, the required terms y_{s_x} and $y_{s_{xx}}$ will be discontinuous where the body curvature is discontinuous. By formulating the shock point solution in terms of the shock slope, σ, which is continuous across surface curvature discontinuities, this difficulty may be avoided.

APPENDIX D. FORCE AND MOMENT INTEGRATION

The resultant forces and moments acting on the vehicle may be determined once the surface pressure distribution has been calculated. The forces and moments may be resolved into components relative to a vehicle-fixed coordinate system, as shown in Figure 4, where

F_A = axial force

F_N = normal force

F_Y = side force

M_X = pitching moment

M_Y = yawing moment

M_Z = rolling moment.

The integrals required for the calculation of these forces and moments may be expressed in terms of the 3DSAP nose geometry coordinate system as

$$F_A = \int_{z_0}^{z}\int_{0}^{2\pi} (p-p_\infty)\hat{r}_b\left[\hat{r}_{b_z} + d_1'\cos\hat{\phi} + d_2'\sin\hat{\phi} + \frac{\hat{r}_{b\hat{\phi}}}{\hat{r}_b}\left(d_1'\sin\hat{\phi} - d_2'\cos\hat{\phi}\right)\right] d\hat{\phi}\, dz \qquad \text{(D.1)}$$

$$F_N = -\int_{z_0}^{z}\int_{0}^{2\pi} p\hat{r}_b\left(\cos\hat{\phi} + \frac{\hat{r}_{b\hat{\phi}}}{\hat{r}_b}\sin\hat{\phi}\right) d\hat{\phi}\, dz \qquad \text{(D.2)}$$

$$F_Y = -\int_{z_0}^{z}\int_{0}^{2\pi} p\hat{r}_b\left(\sin\hat{\phi} - \frac{\hat{r}_{b\hat{\phi}}}{\hat{r}_b}\cos\hat{\phi}\right) d\hat{\phi}\, dz \qquad \text{(D.3)}$$

$$M_x = \int_{z_0}^{z}\int_{0}^{2\pi} p\hat{r}_b z\left(\cos\hat{\phi} + \frac{\hat{r}_{b\hat{\phi}}}{\hat{r}_b}\sin\hat{\phi}\right) d\hat{\phi}dz$$
$$+ \int_{z_0}^{z}\int_{0}^{2\pi} (p-p_\infty)\hat{r}_b\left(\hat{r}_b\cos\hat{\phi} + d_1\right)\left[\hat{r}_{b_z} + d_1'\cos\hat{\phi} + d_2'\sin\hat{\phi}\right.$$
$$\left. + \frac{\hat{r}_{b\hat{\phi}}}{\hat{r}_b}\left(d_1'\sin\hat{\phi} - d_2'\cos\hat{\phi}\right)\right] d\hat{\phi}dz + \bar{Z}F_N - \bar{Y}F_A \qquad \text{(D.4)}$$

$$M_Y = \int_{z_0}^{z}\int_{0}^{2\pi} p\hat{r}_b z\left(\sin\hat{\phi} - \frac{\hat{r}_{b\hat{\phi}}}{\hat{r}_b}\cos\hat{\phi}\right) d\hat{\phi}dz$$
$$+ \int_{z_0}^{z}\int_{0}^{2\pi} (p-p_\infty)\hat{r}_b\left(\hat{r}_b\sin\hat{\phi} + d_2\right)\left[\hat{r}_{b_z} + d_1'\cos\hat{\phi} + d_2'\sin\hat{\phi}\right.$$
$$\left. + \frac{\hat{r}_{b\hat{\phi}}}{\hat{r}_b}\left(d_1'\sin\hat{\phi} - d_2'\cos\hat{\phi}\right)\right] d\hat{\phi}dz + \bar{Z}F_Y - \bar{X}F_A \qquad \text{(D.5)}$$

$$M_Z = -\int_{z_0}^{z}\int_{0}^{2\pi} p\hat{r}_b\left(\hat{r}_b\cos\hat{\phi} + d_1\right)\left(\sin\hat{\phi} - \frac{\hat{r}_{b\hat{\phi}}}{\hat{r}_b}\cos\hat{\phi}\right) d\hat{\phi}dz$$
$$+ \int_{z_0}^{z}\int_{0}^{2\pi} p\hat{r}_b\left(\hat{r}_b\sin\hat{\phi} + d_2\right)\left(\cos\hat{\phi} + \frac{\hat{r}_{b\hat{\phi}}}{\hat{r}_b}\sin\hat{\phi}\right) d\hat{\phi}dz \qquad \text{(D.6)}$$
$$- \bar{Y}F_Y + \bar{X}F_N$$

where $\bar{X}, \bar{Y}, \bar{Z}$ defines the location of the moment reference point.

In the numerical integration of the above equations on the nose, circumferential variations are approximated using cubic spline functions. The axial integration is carried out using the trapezoidal rule. In 3DSAP, the base pressure is assumed to be p_∞.

On the axisymmetric frustum, where $\hat{r}_{b_{\hat{\phi}}} = d_1 = d_2 = d_1' = d_2' = 0$, and $\hat{r}_{b_z} = \tan\theta_b$, the above integrals reduce to

$$F_A = \int_{z_f}^{z} r_b \tan\theta_b \int_{0}^{2\pi} (p-p_\infty)\, d\phi dz \qquad \text{(D.7)}$$

$$F_N = -\int_{z_f}^{z} r_b \int_0^{2\pi} p \cos\phi \, d\phi \, dz \tag{D.8}$$

$$F_Y = -\int_{z_f}^{z} r_b \int_0^{2\pi} p \sin\phi \, d\phi \, dz \tag{D.9}$$

$$M_X = \int_{z_f}^{z} r_b z \int_0^{2\pi} p \cos\phi \, d\phi \, dz + \int_{z_f}^{z} r_b^2 \tan\theta_b \int_0^{2\pi} (p - p_\infty) \cos\phi \, d\phi \, dz + \bar{z} F_N - \bar{Y} F_A \tag{D.10}$$

$$M_Y = \int_{z_f}^{z} r_b z \int_0^{2\pi} p \sin\phi \, d\phi \, dz + \int_{z_f}^{z} r_b^2 \tan\theta_b \int_0^{2\pi} (p - p_\infty) \sin\phi \, d\phi \, dz + \bar{z} F_Y - \bar{X} F_A \tag{D.11}$$

$$M_Z = -\bar{Y} F_Y + \bar{X} F_N . \tag{D.12}$$

These frustum integrals may be further simplified by assuming the functional form of the circumferential pressure distribution at each axial station and analytically carrying out the integration in ϕ. The general form of the assumed pressure distribution is

$$p(\phi) = p_1 + p_2 \cos(\phi + \Gamma) + p_3 \cos(2\phi + 2\Gamma) \quad , \quad -\Gamma \le \phi \le \pi - \Gamma \tag{D.13}$$

$$p(\phi) = p_4 + p_5 \cos(\phi + \Gamma) + p_6 \cos(2\phi + 2\Gamma) \quad , \quad \pi - \Gamma \le \phi \le 2\pi - \Gamma$$

where

$$p_1 = \frac{1}{4}\left[p(-\Gamma) + 2p\left(\frac{\pi}{2} - \Gamma\right) + p(\pi - \Gamma)\right]$$

$$p_2 = \frac{1}{2}\left[p(-\Gamma) - p(\pi - \Gamma)\right]$$

$$p_3 = \frac{1}{4}\left[p(-\Gamma) - 2p\left(\frac{\pi}{2} - \Gamma\right) + p(\pi - \Gamma)\right]$$

$$p_4 = \frac{1}{4}\left[p(\pi - \Gamma) + 2p\left(\frac{3\pi}{2} - \Gamma\right) + p(-\Gamma)\right]$$

$$p_5 = \frac{1}{2}\left[p(-\Gamma) - p(\pi - \Gamma)\right] = p_1$$

$$p_6 = \frac{1}{4}\left[p(\pi - \Gamma) - 2p\left(\frac{3\pi}{2} - \Gamma\right) + p(-\Gamma)\right]$$

With this pressure distribution, the frustum integrals reduce to

$$F_A = \pi \int_{z_f}^{z} (p_1 + p_4 - p_b) r_b \tan\theta_b \, dz \qquad \text{(D. 14)}$$

$$F_N = -\int_{z_f}^{z} r_b A(z) \, dz \qquad \text{(D. 15)}$$

$$F_Y = -\int_{z_f}^{z} r_b B(z) \, dz \qquad \text{(D. 16)}$$

$$M_x = \int_{z_f}^{z} r_b (z + r_b \tan\theta_b) A(z) \, dz + \bar{z} F_N - \bar{Y} F_A \qquad \text{(D. 17)}$$

$$M_Y = \int_{z_f}^{z} r_b (z + r_b \tan\theta_b) B(z) \, dz + \bar{z} F_Y - \bar{X} F_A \qquad \text{(D. 18)}$$

$$M_z = -\bar{Y} F_Y + \bar{X} F_N \qquad \text{(D. 19)}$$

where

$$A(z) = 2(p_1 - p_4)\sin\Gamma + \frac{\pi}{2}(p_2 + p_5)\cos\Gamma$$
$$+ (p_3 + p_6)\left[\cos 2\Gamma\left(\sin\Gamma + \tfrac{1}{3}\sin 3\Gamma\right)\right.$$
$$\left. - \sin 2\Gamma\left(\cos\Gamma + \tfrac{1}{3}\cos 3\Gamma\right)\right]$$

$$B(z) = 2(p_1 - p_4)\cos\Gamma - \frac{\pi}{2}(p_2 + p_5)\sin\Gamma$$
$$+ (p_3 - p_6)\left[\cos 2\Gamma\left(-\cos\Gamma + \tfrac{1}{3}\cos 3\Gamma\right)\right.$$
$$\left. - \sin 2\Gamma\left(\sin\Gamma - \tfrac{1}{3}\sin 3\Gamma\right)\right.$$

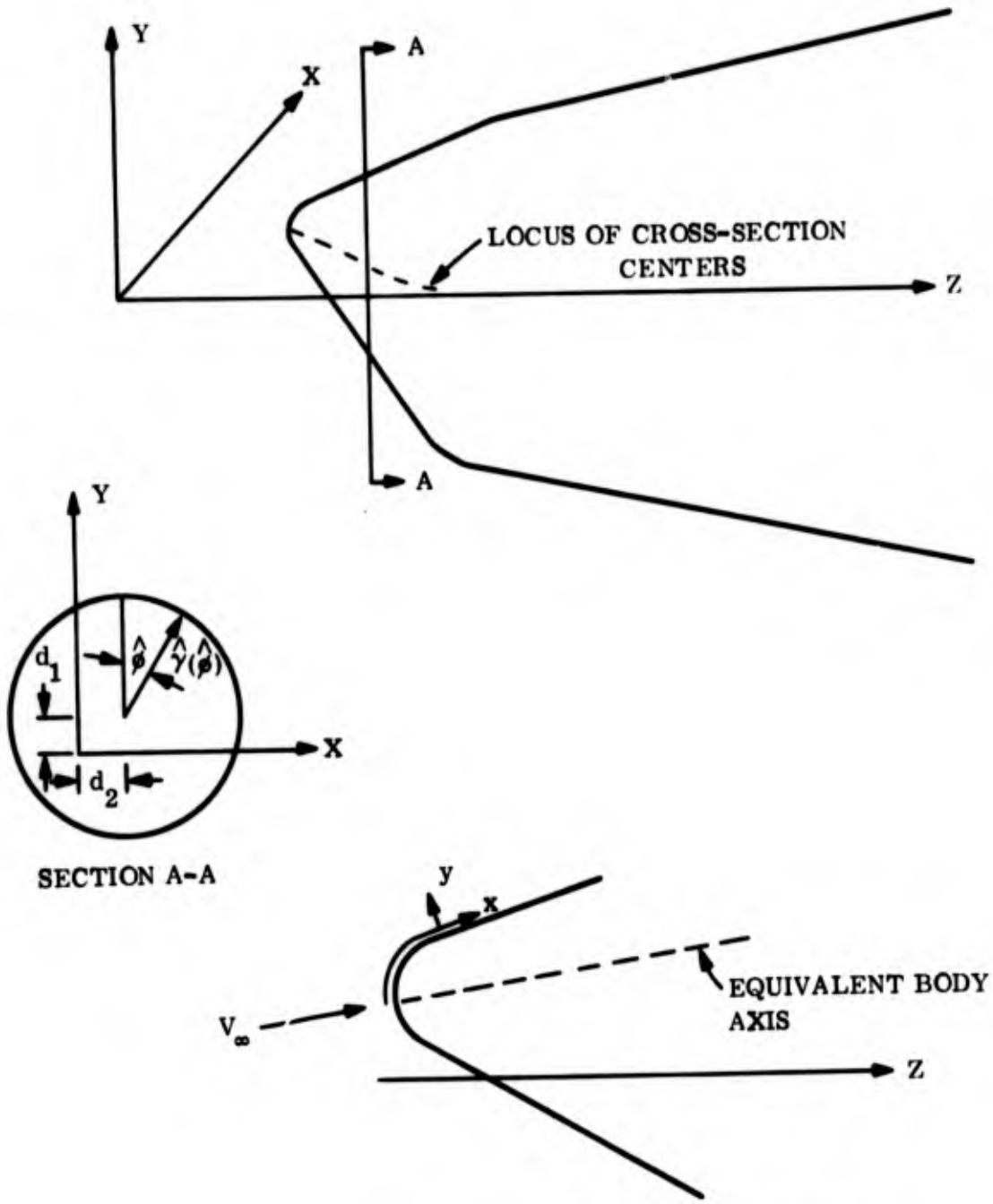

BODY-NORMAL COORDINATE SYSTEM

Figure 1. 3DSAP Nose Geometry

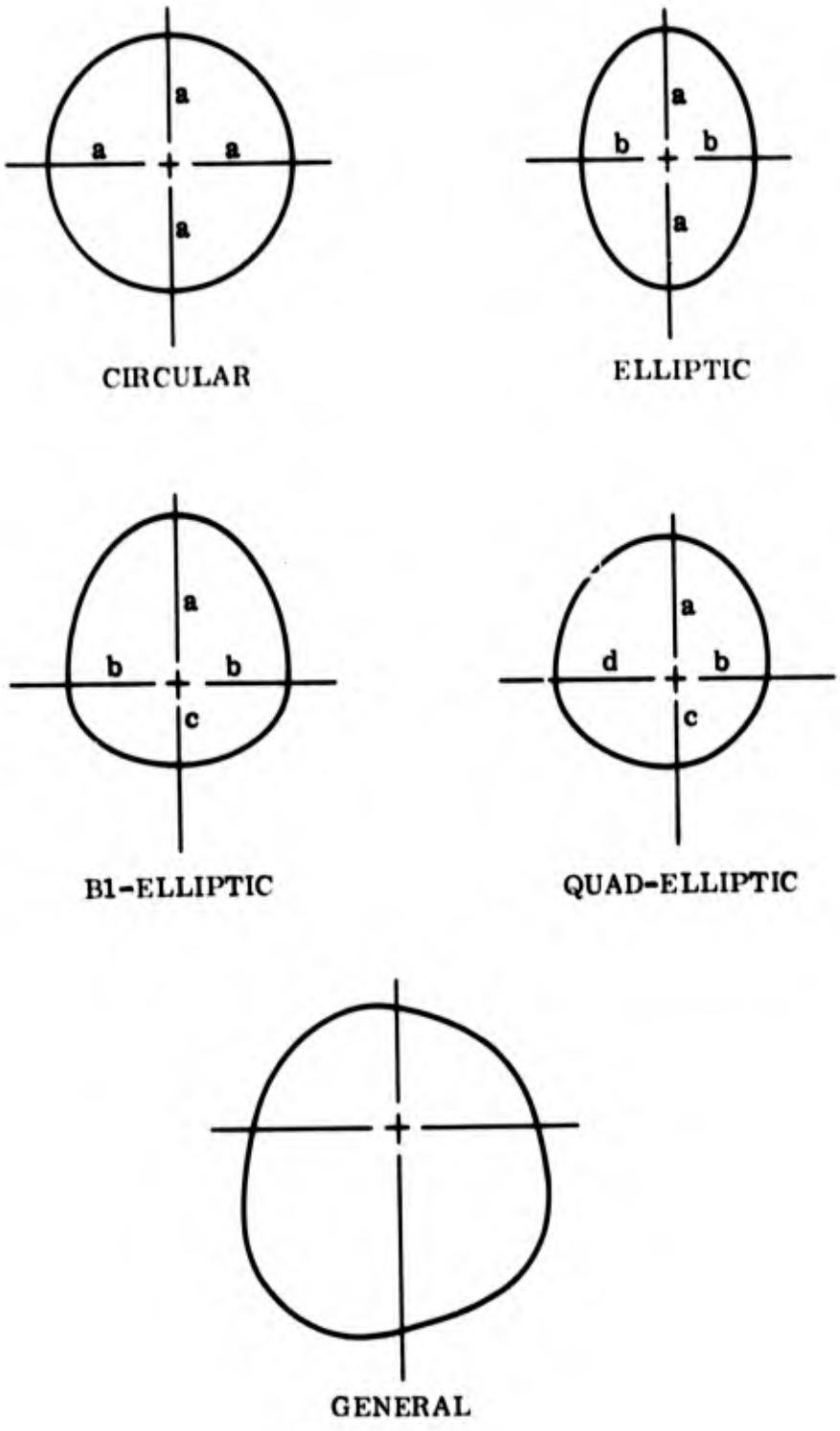

Figure 2. 3DSAP Nose Cross-Sections

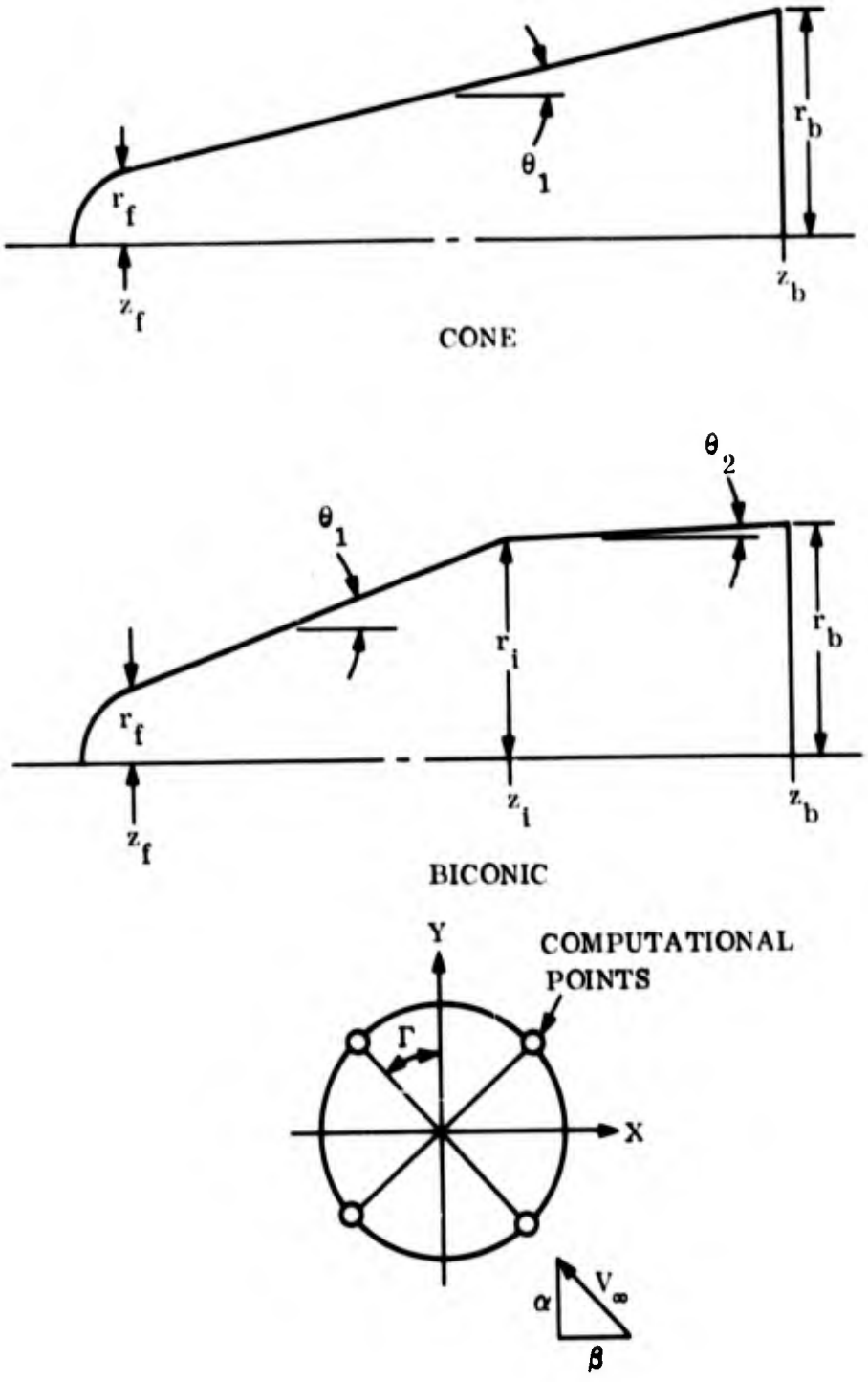

Figure 3. 3DSAP Frustum Geometry

α: POSITIVE NOSE UP

β: POSITIVE NOSE LEFT

SYMMETRIC VEHICLE

$+\alpha \Rightarrow +C_N, -C_m$

$+\beta \Rightarrow -C_Y, +C_n$

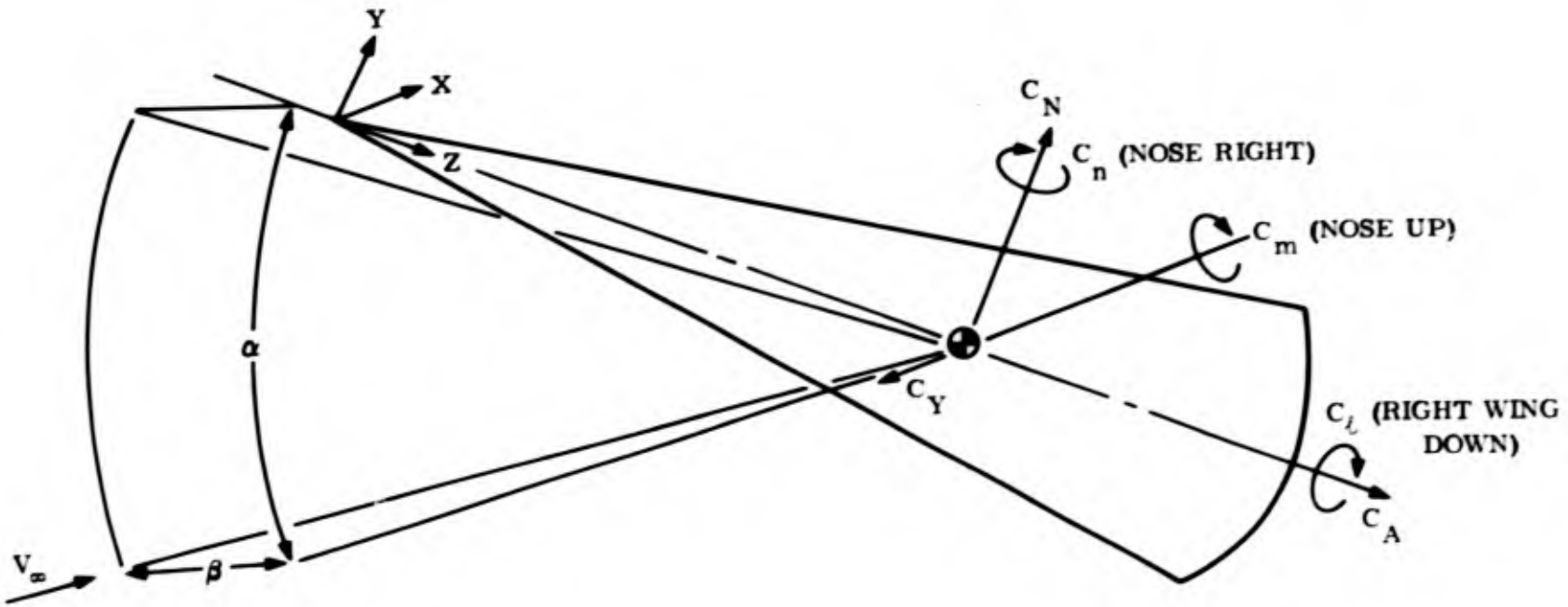

Figure 4. 3DSAP Sign Conventions

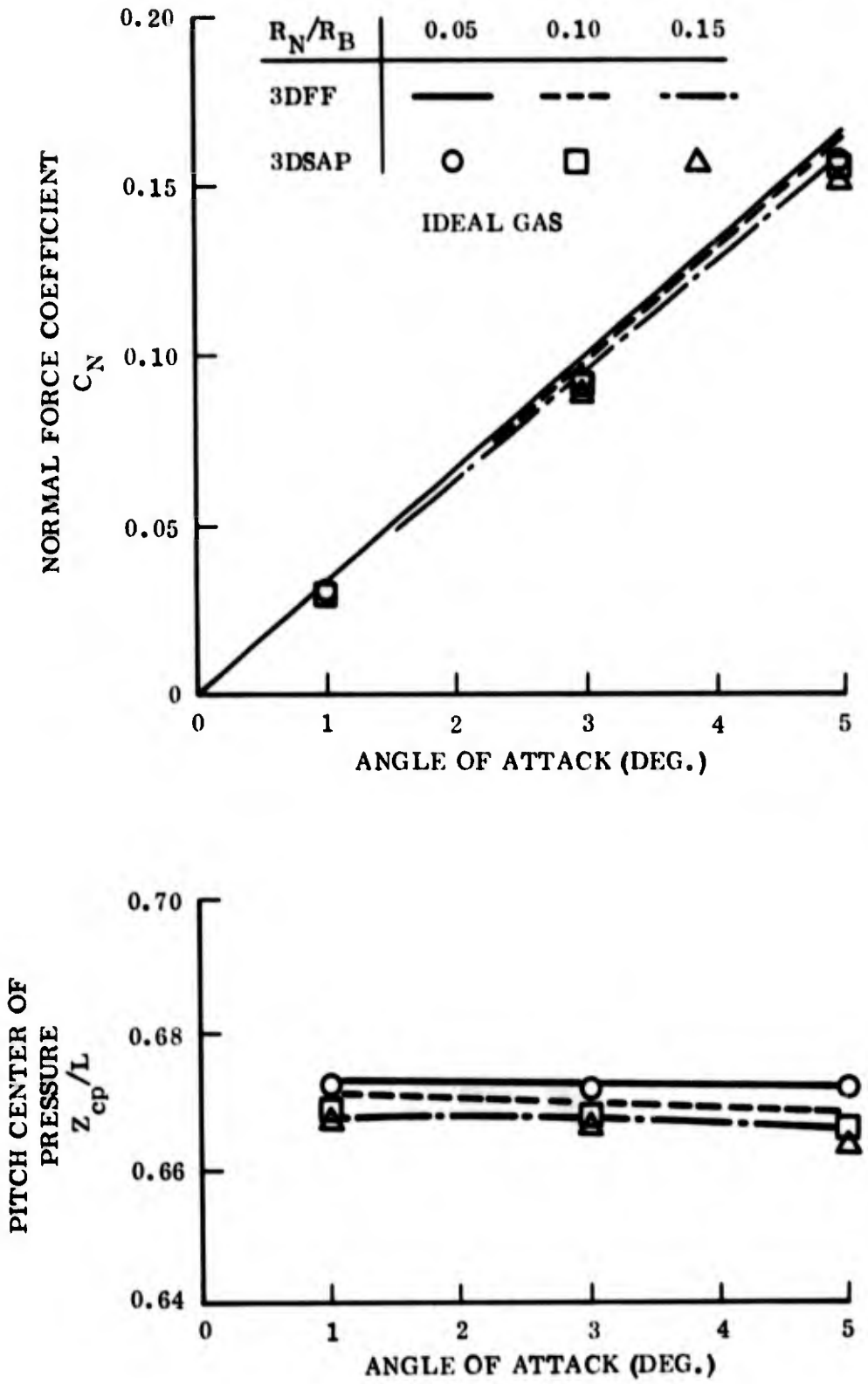

Figure 5. Normal Force Coefficient and Pitch Center of Pressure for 9^{o} Sphere-Cone at $M_{\infty} = 5$

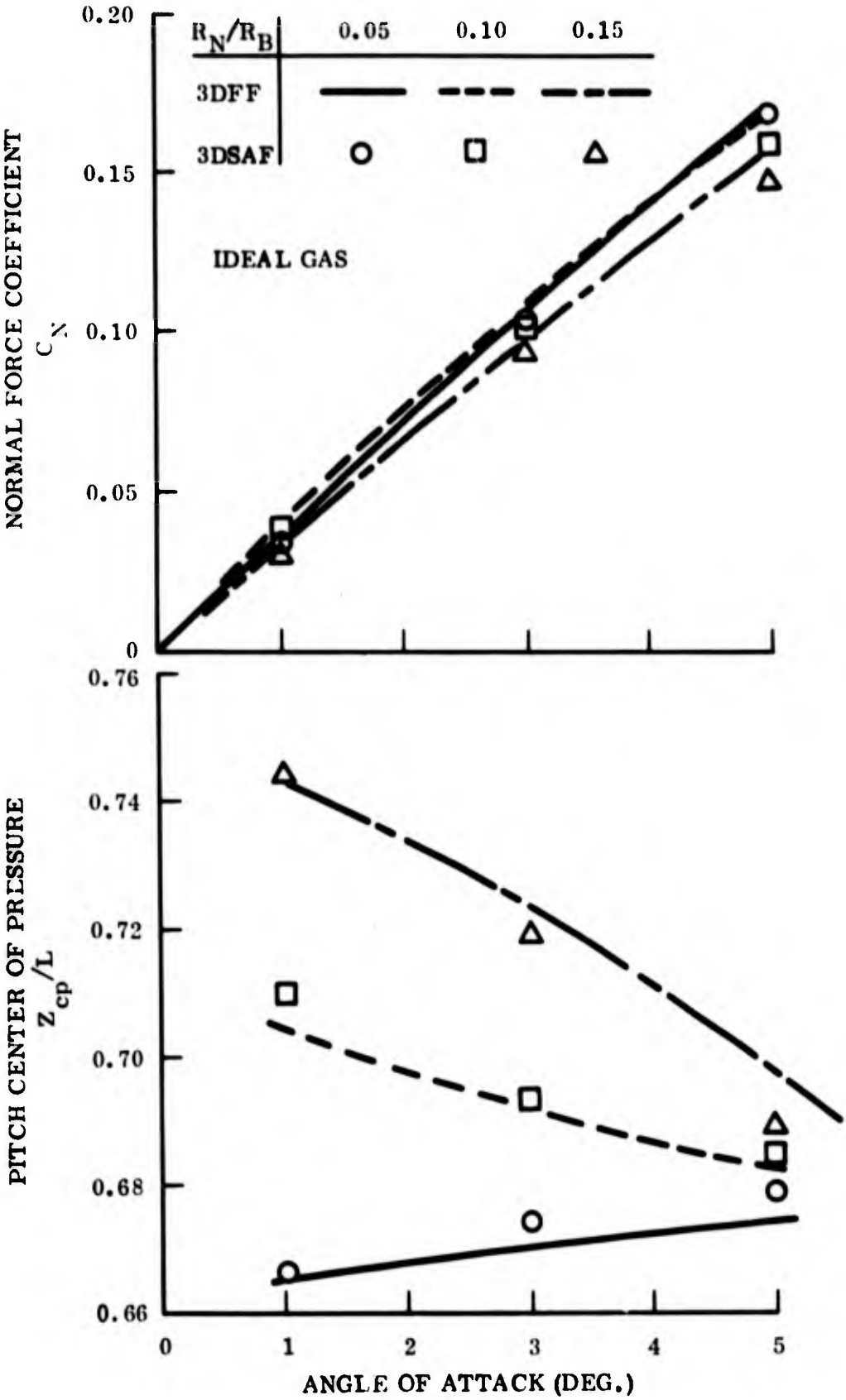

Figure 6. Normal Force Coefficient and Pitch Center of Pressure for 9^{o} Sphere-Cone at $M_{\infty} = 20$

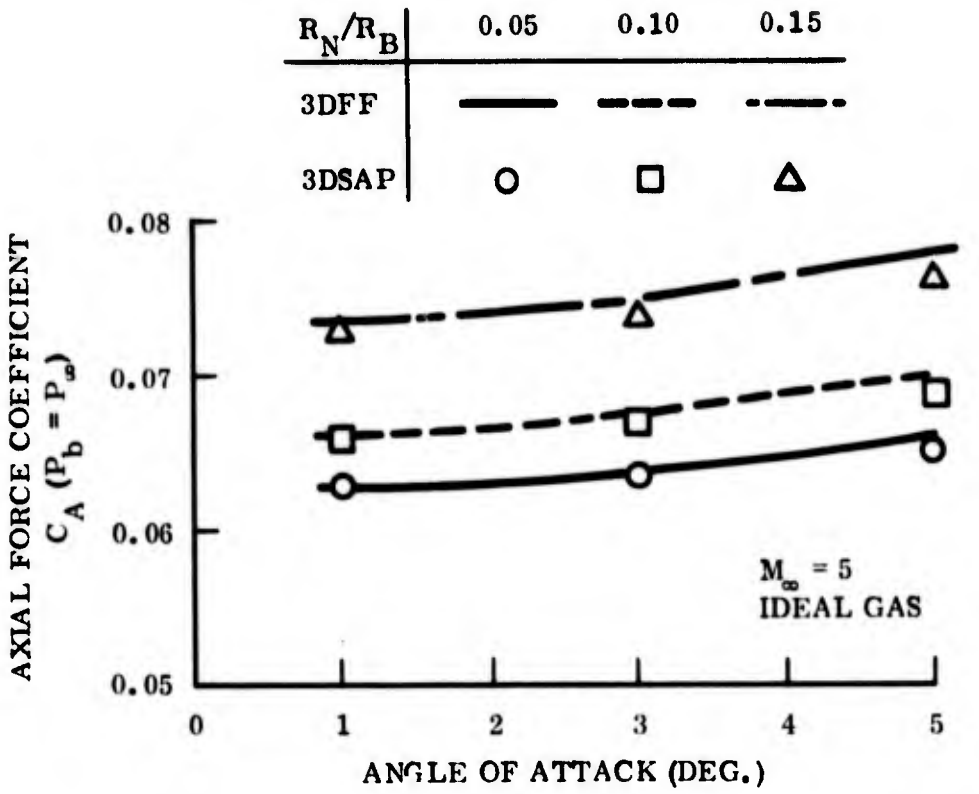

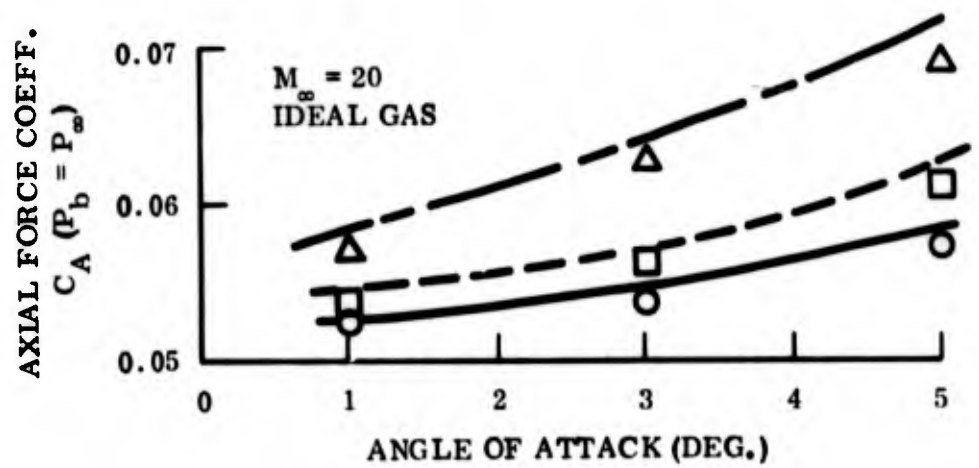

Figure 7. Axial Force Coefficient for 9^o Sphere-Cone at $M_\infty = 5, 20$

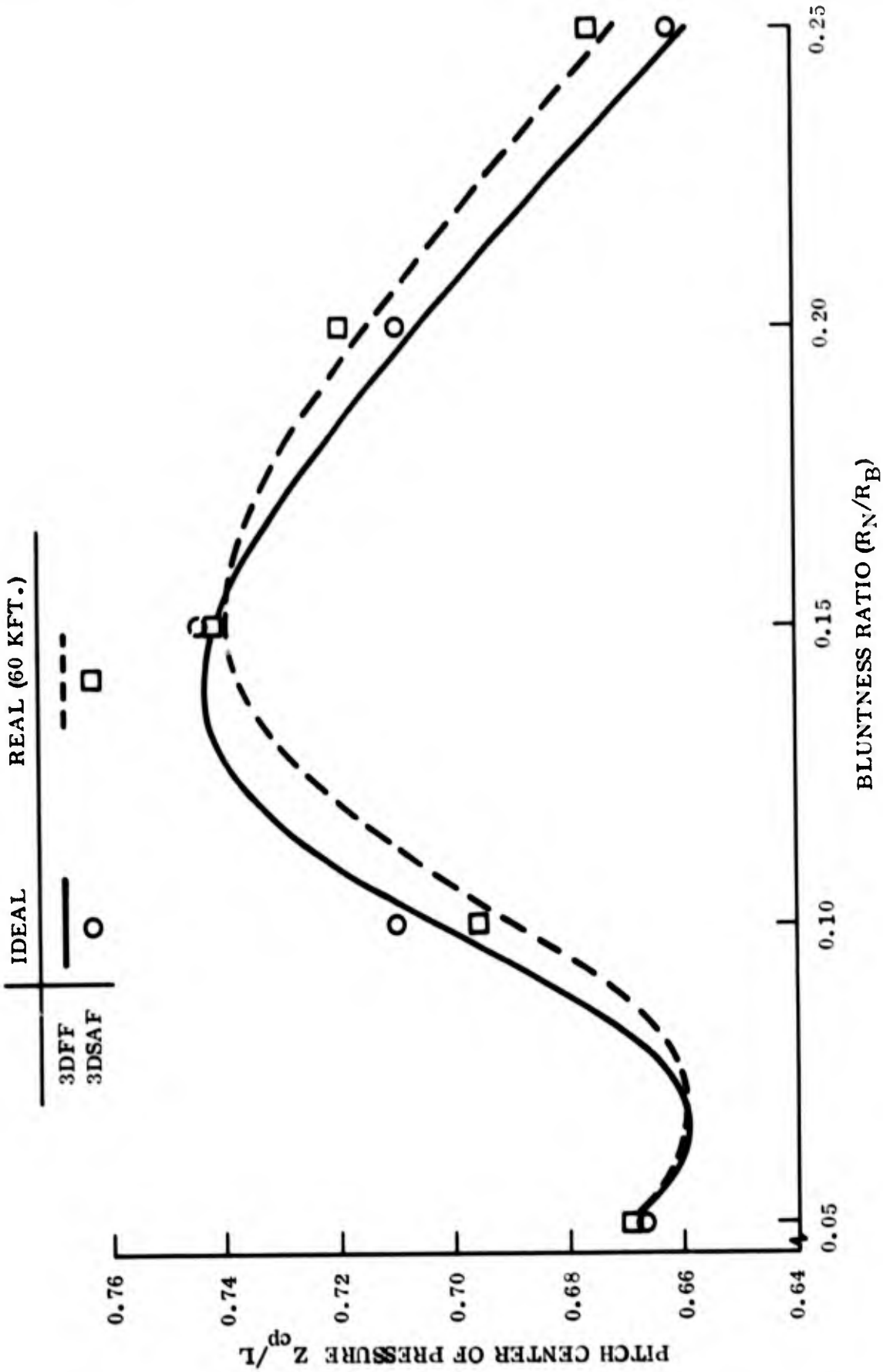

Figure 8. Pitch Center of Pressure versus Bluntness
9° Sphere-Cone $M_\infty = 20$ $\alpha = 1°$

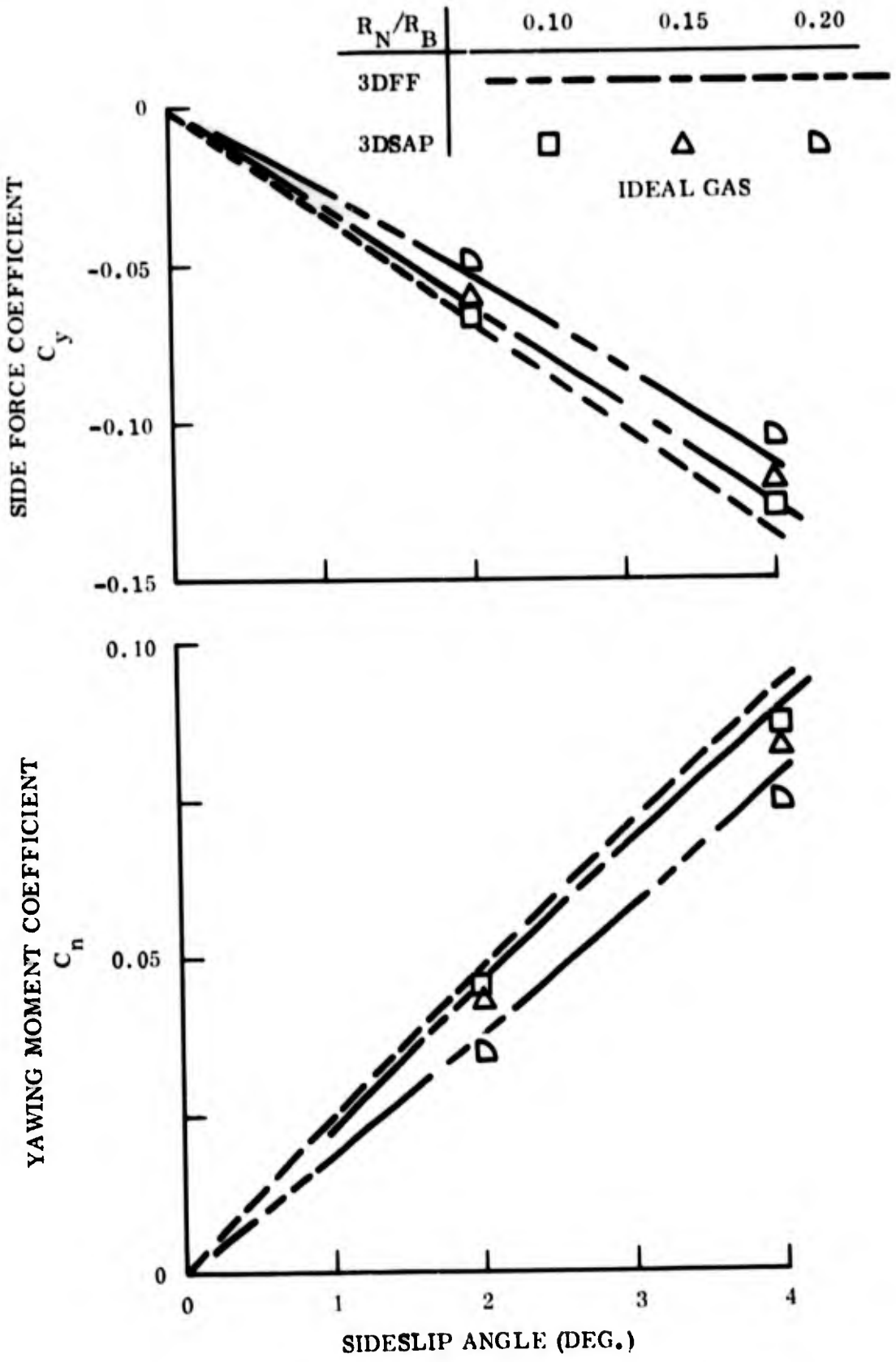

Figure 9. Side Force and Yawing Moment Coefficients for 9° Sphere-Cone at $M_{\infty} = 10$ and $\alpha = 1^{\circ}$

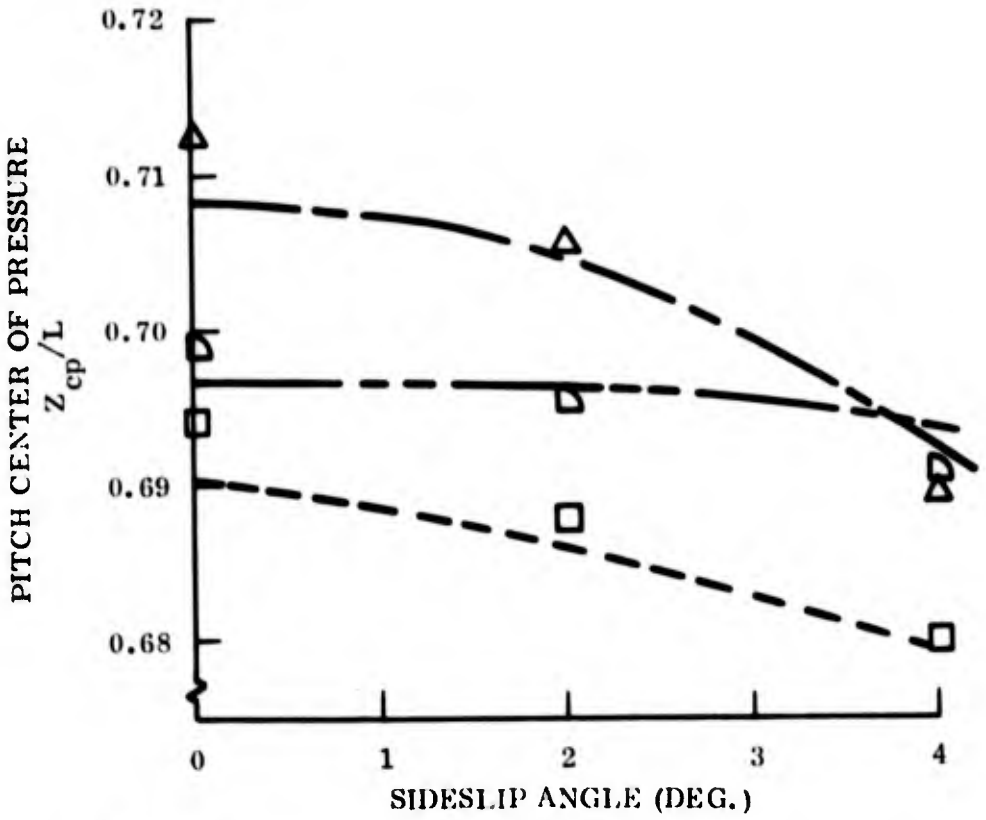

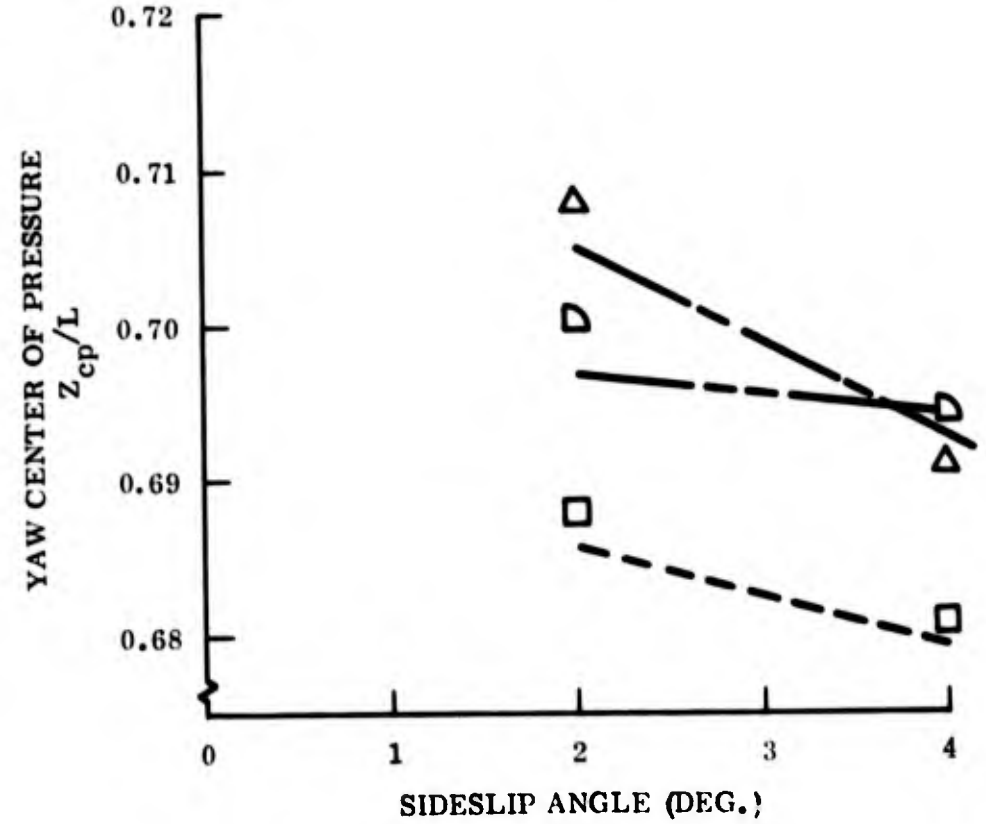

Figure 10. Pitch and Yaw Centers of Pressure for 9^{o} Sphere-Cone at M_{∞} and $\alpha = 1^{o}$

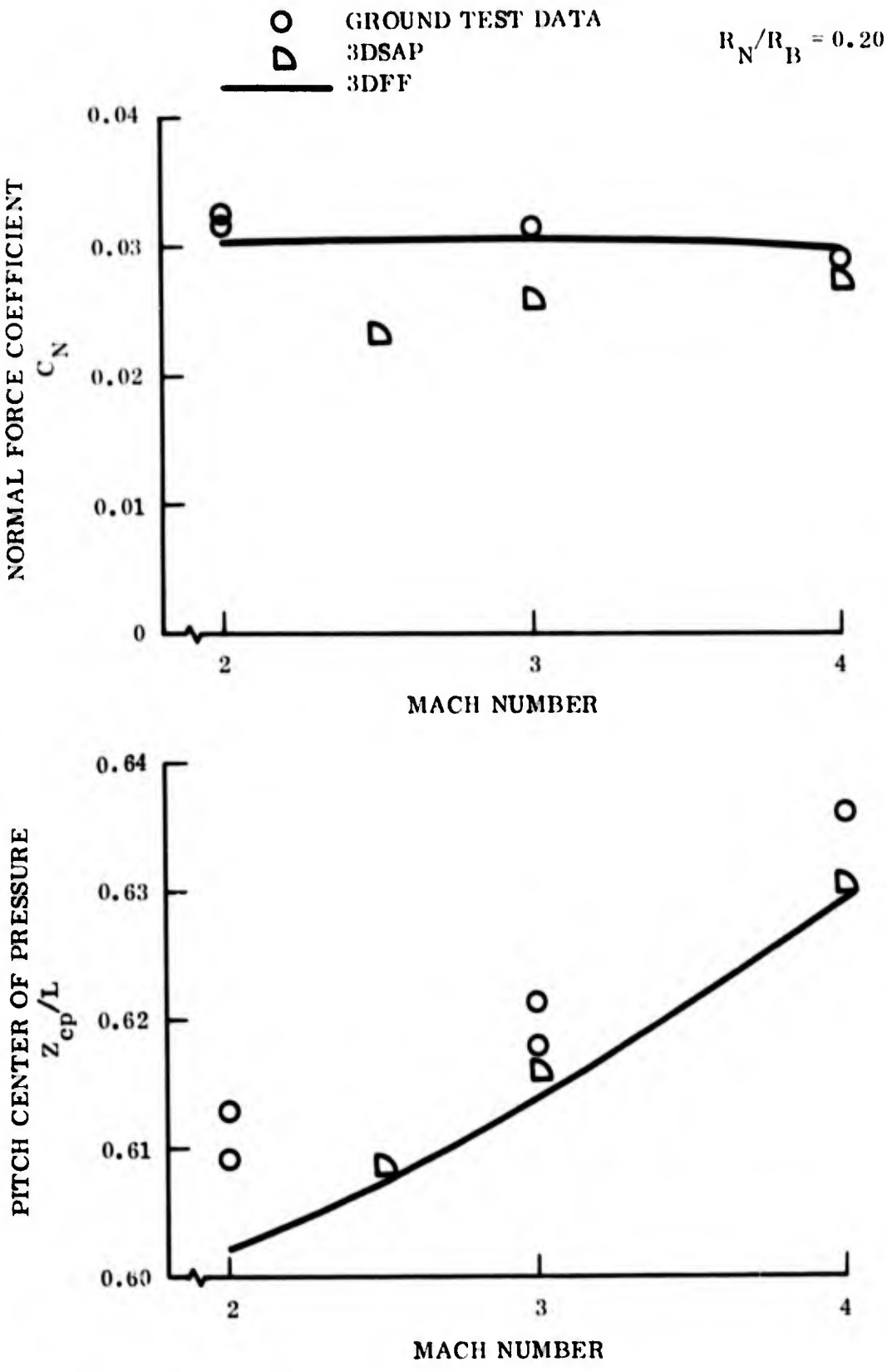

Figure 11. Normal Force Coefficient and Pitch Center of Pressure for 7° Sphere-Cone at $\alpha = 1^{\circ}$ at Low Mach Number

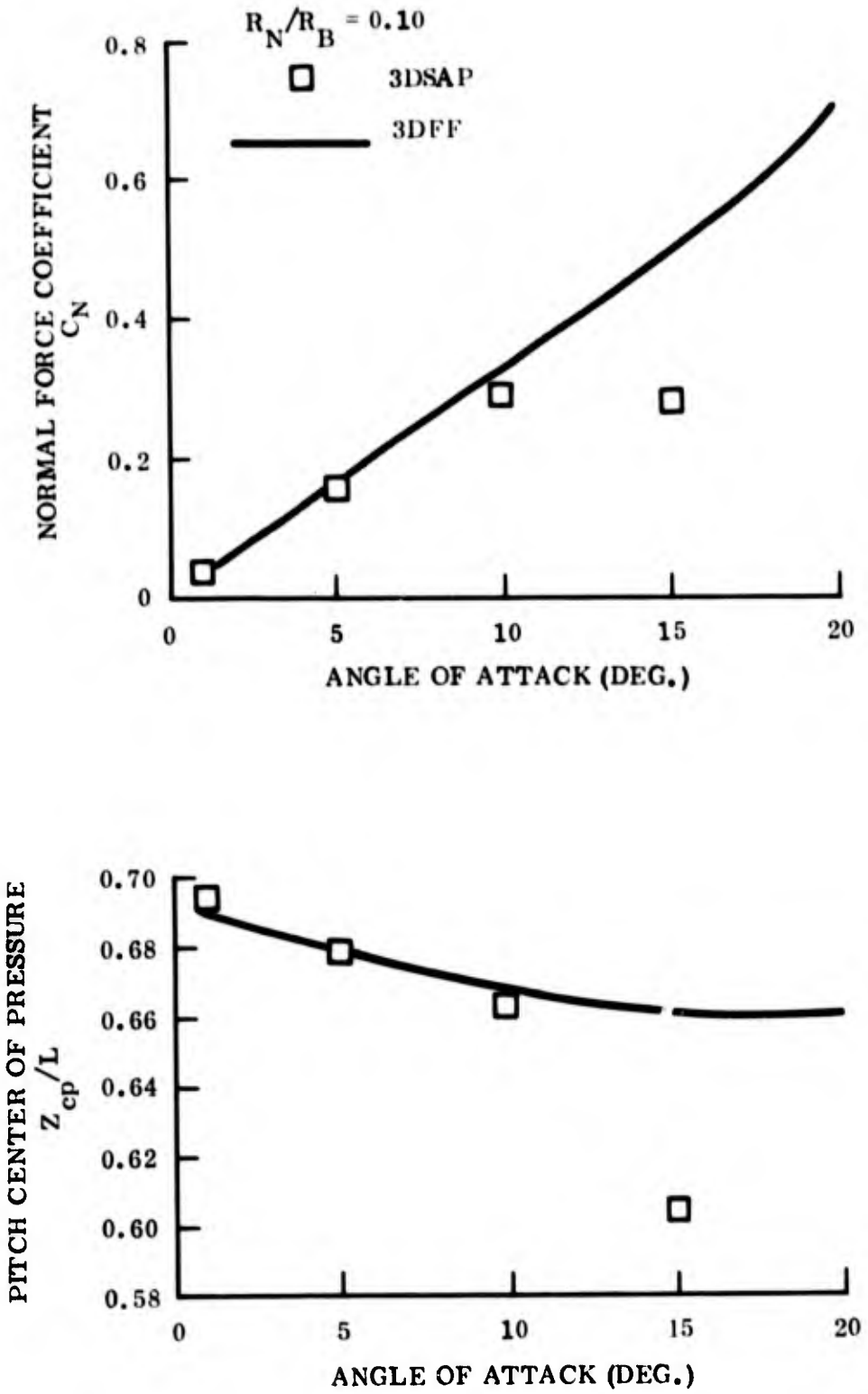

Figure 12. Normal Force Coefficient and Pitch Center of Pressure for a 9° Sphere-Cone at M_∞ = 10 at High α

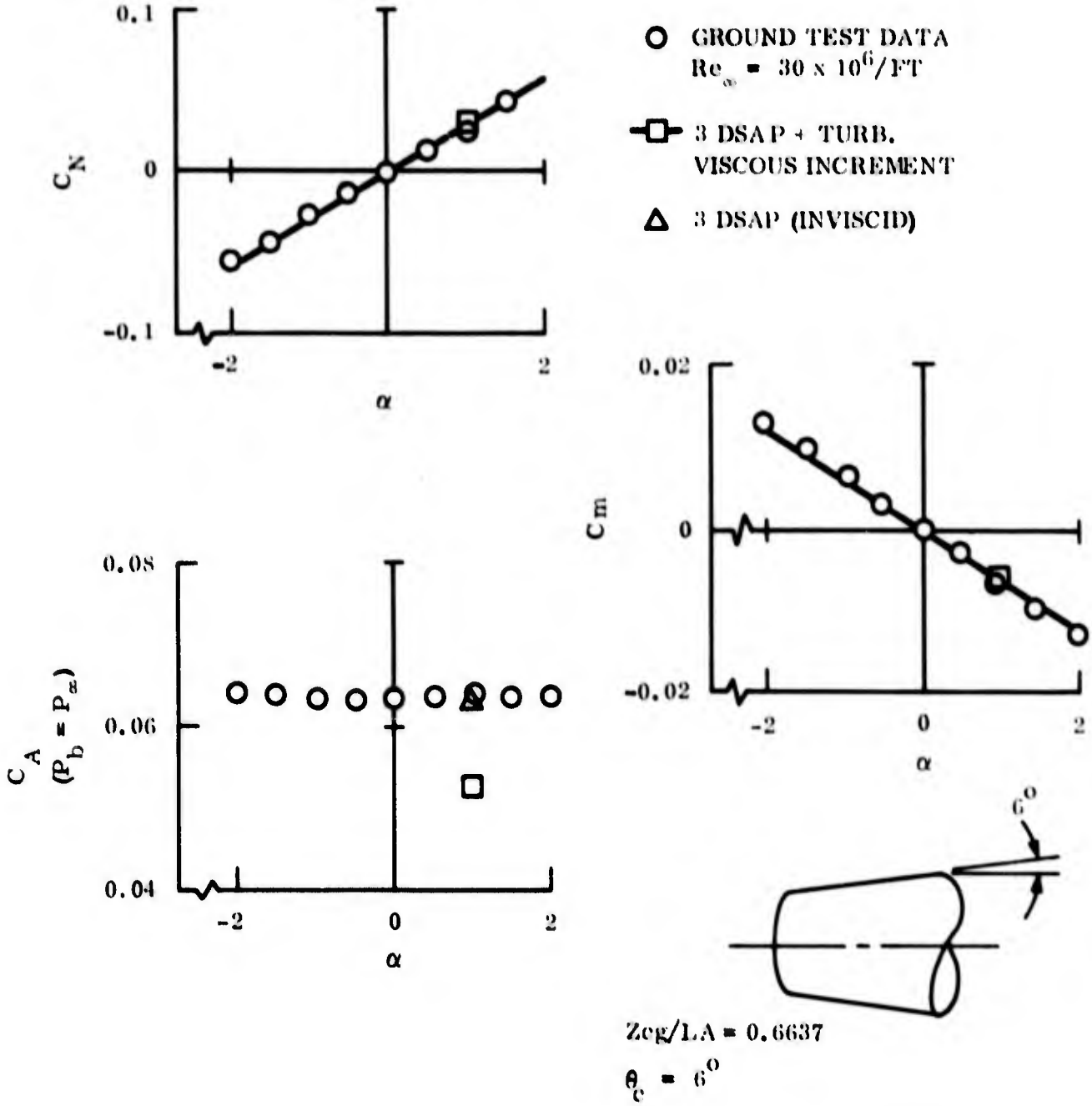

Figure 13. Normal Force, Pitching Moment, and Axial Force Coefficients for Laminar Symmetric Shape at $M_\infty = 5$

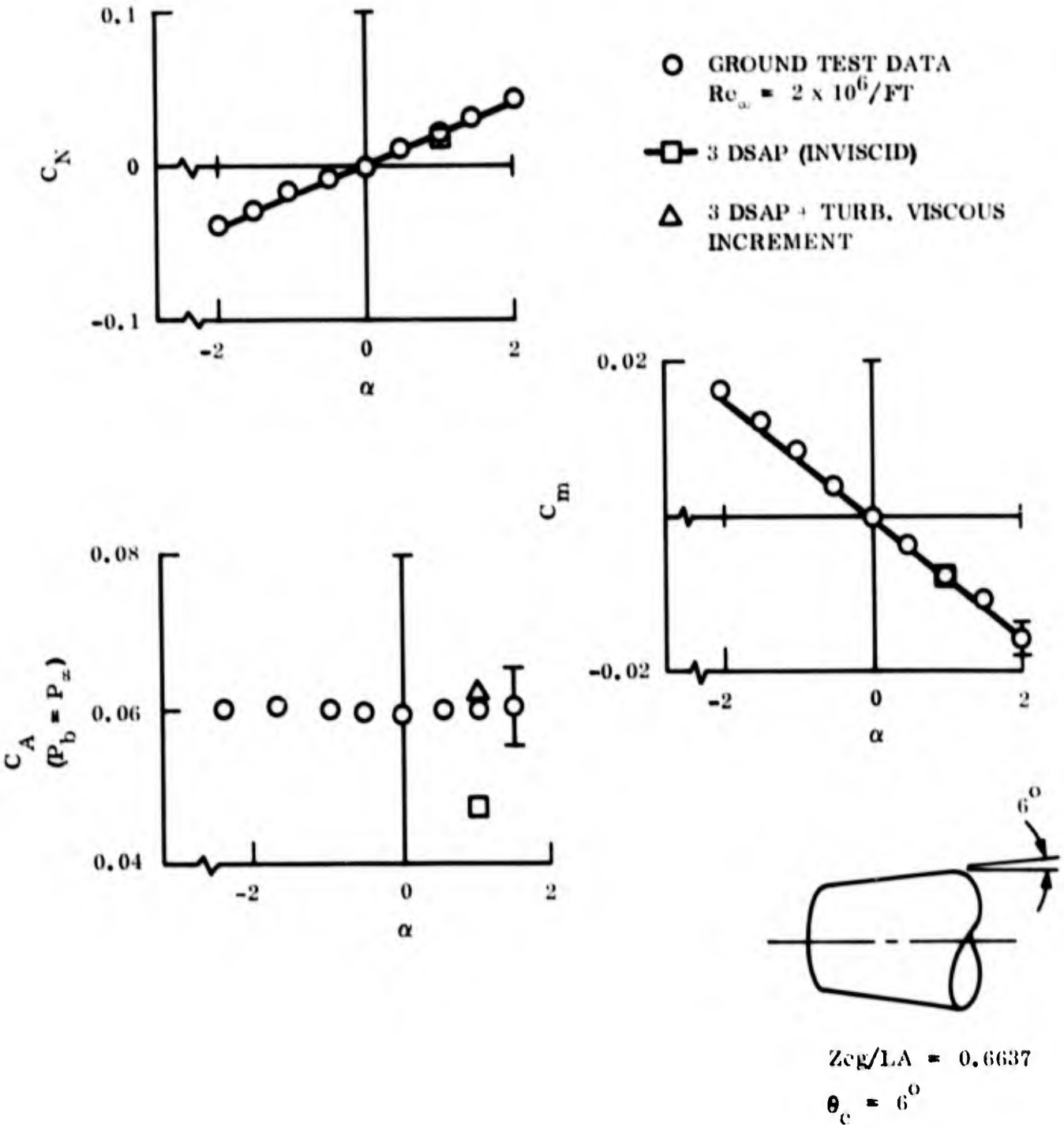

Figure 14. Normal Force, Pitching Moment, and Axial Force Coefficients for Laminar Symmetric Shape at M_∞ = 10

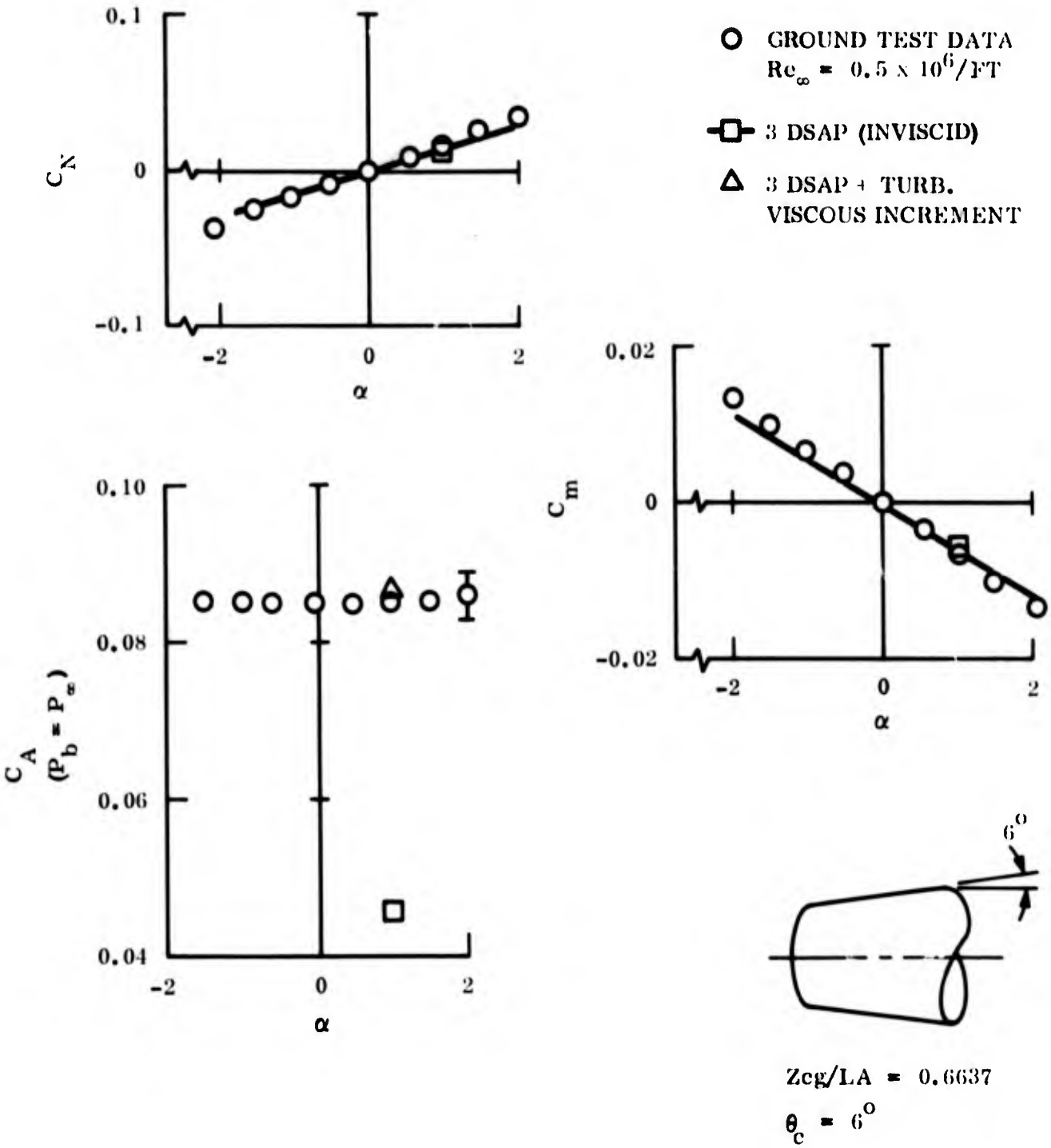

Figure 15. Normal Force, Pitching Moment, and Axial Force Coefficients for Laminar Symmetric Shape at M_∞ = 18

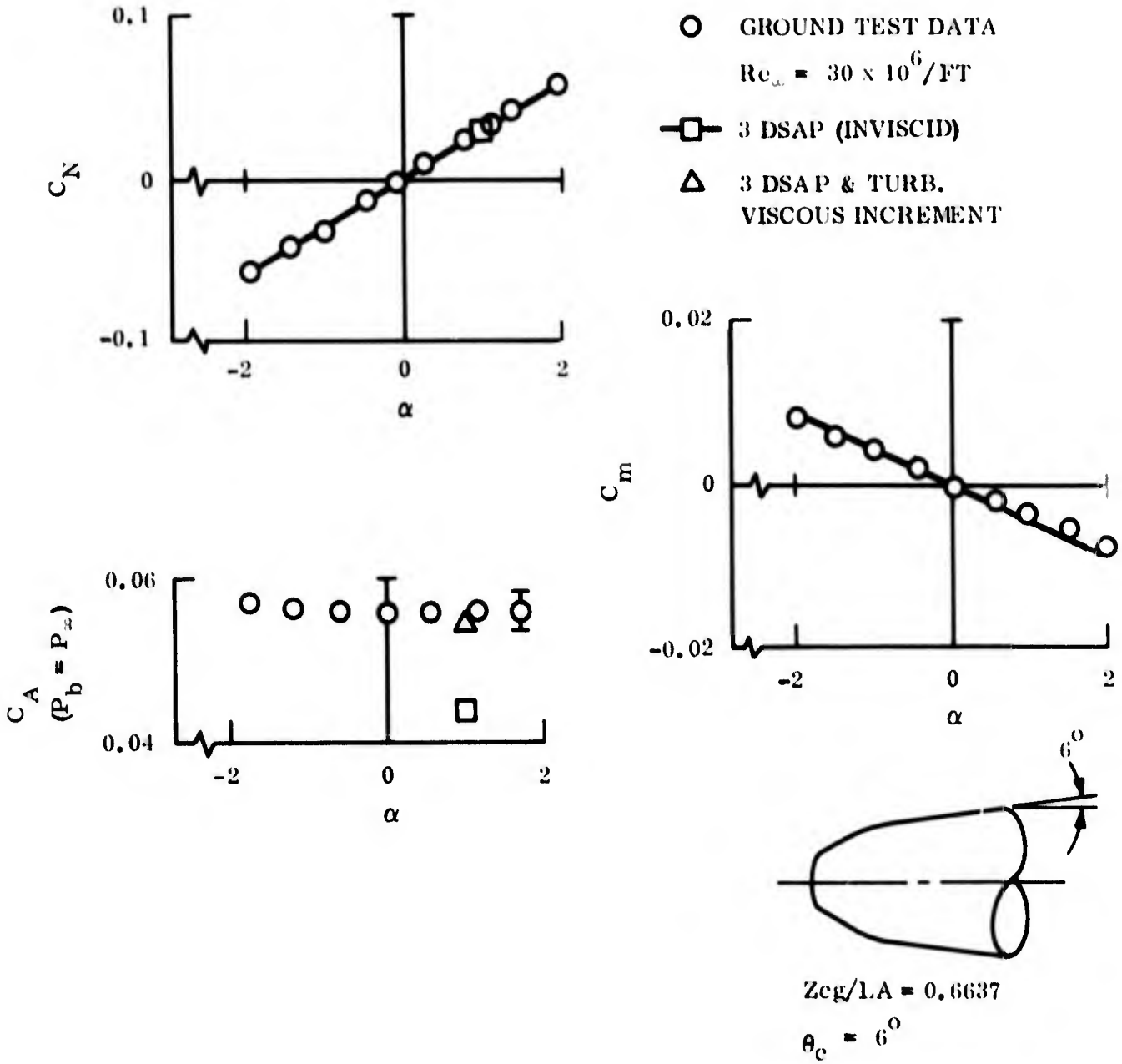

Figure 16. Normal Force, Pitching Moment, and Axial Force Coefficients for Transitional Symmetric Shape at M_∞ = 5

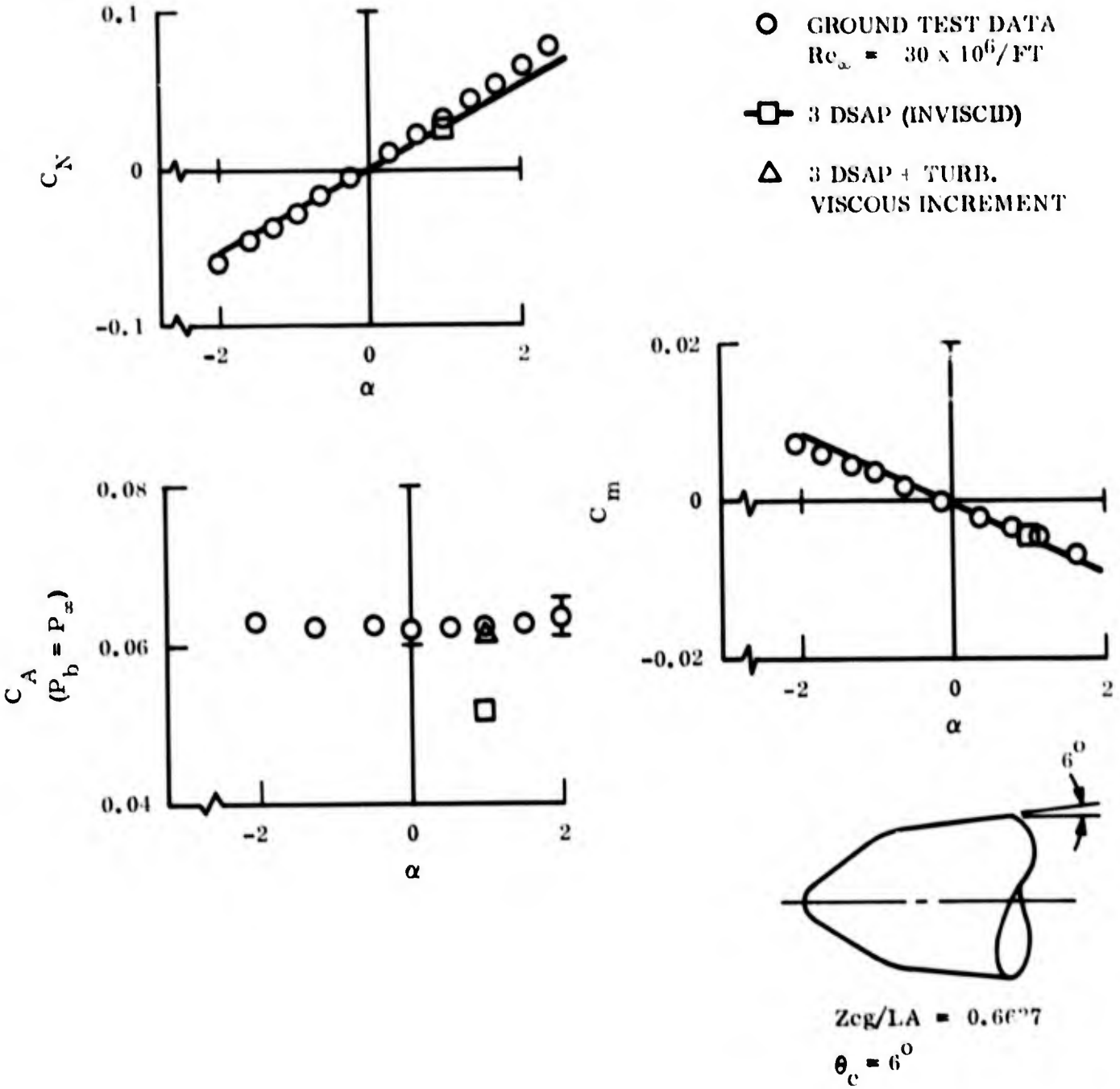

Figure 17. Normal Force, Pitching Moment, and Axial Force Coefficients for Turbulent Symmetric Shape at $M_\infty = 5$

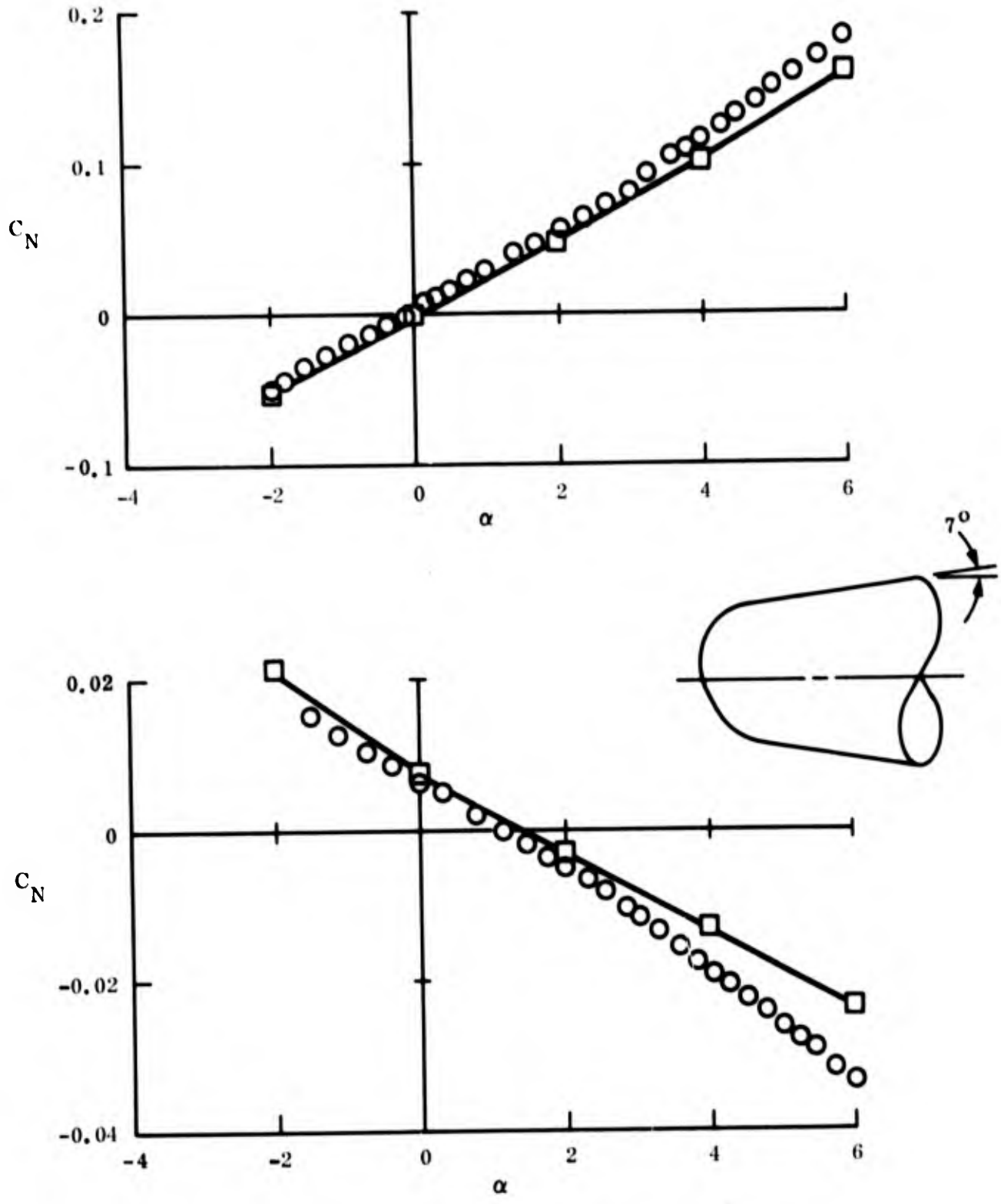

○ GROUND TEST DATA, Re_∞ = 23.7 x 10^6/FT

□ 3 DSAP

Zcg/LA = 0.66

θ_c = 7°

Figure 18. Normal Force and Pitching Moment Coefficients for Laminar Asymmetric Shape at M_∞ = 5

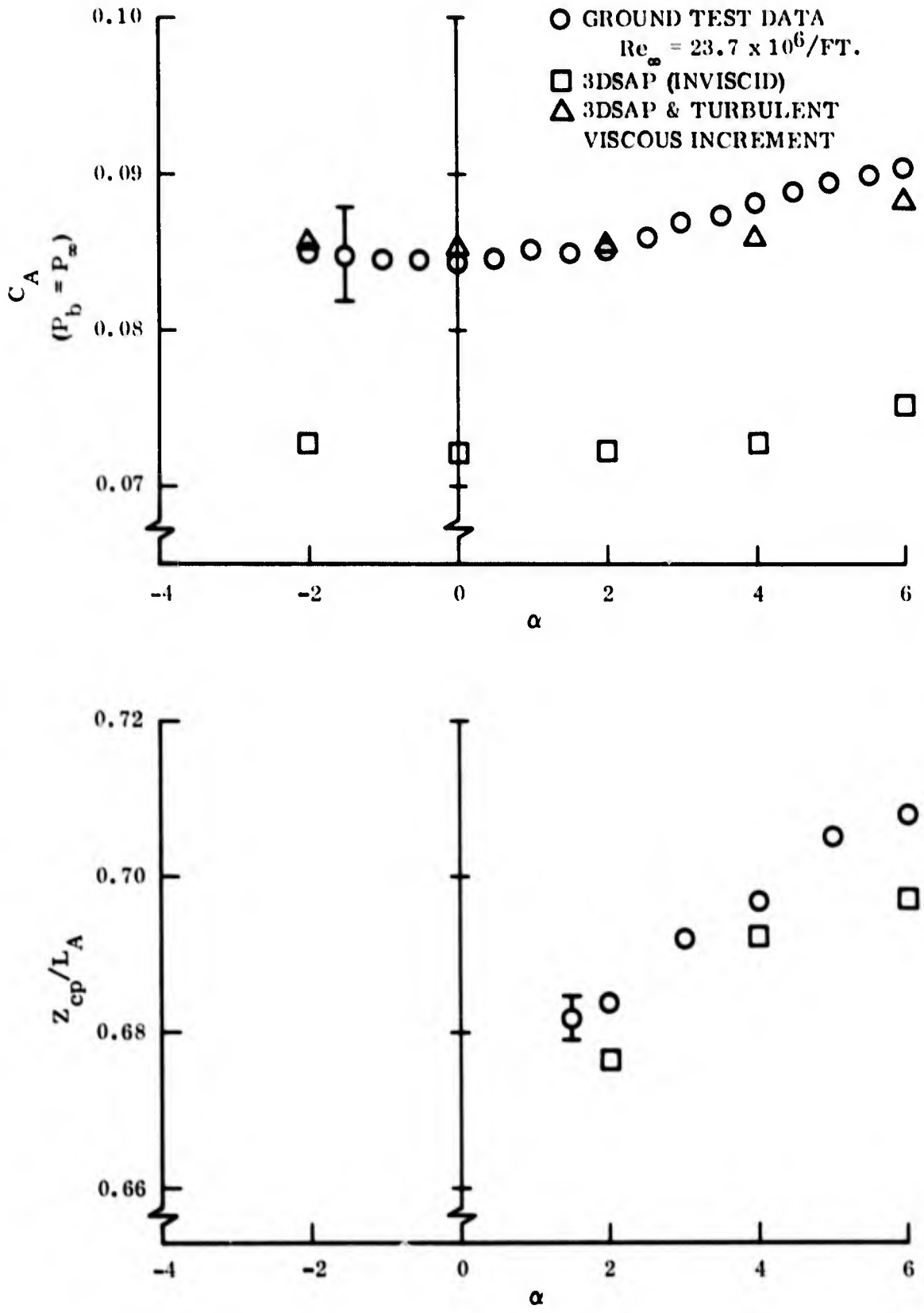

Figure 19. Axial Force Coefficient and Pitch Center of Pressure for Laminar Asymmetric Shape at $M_\infty = 5$

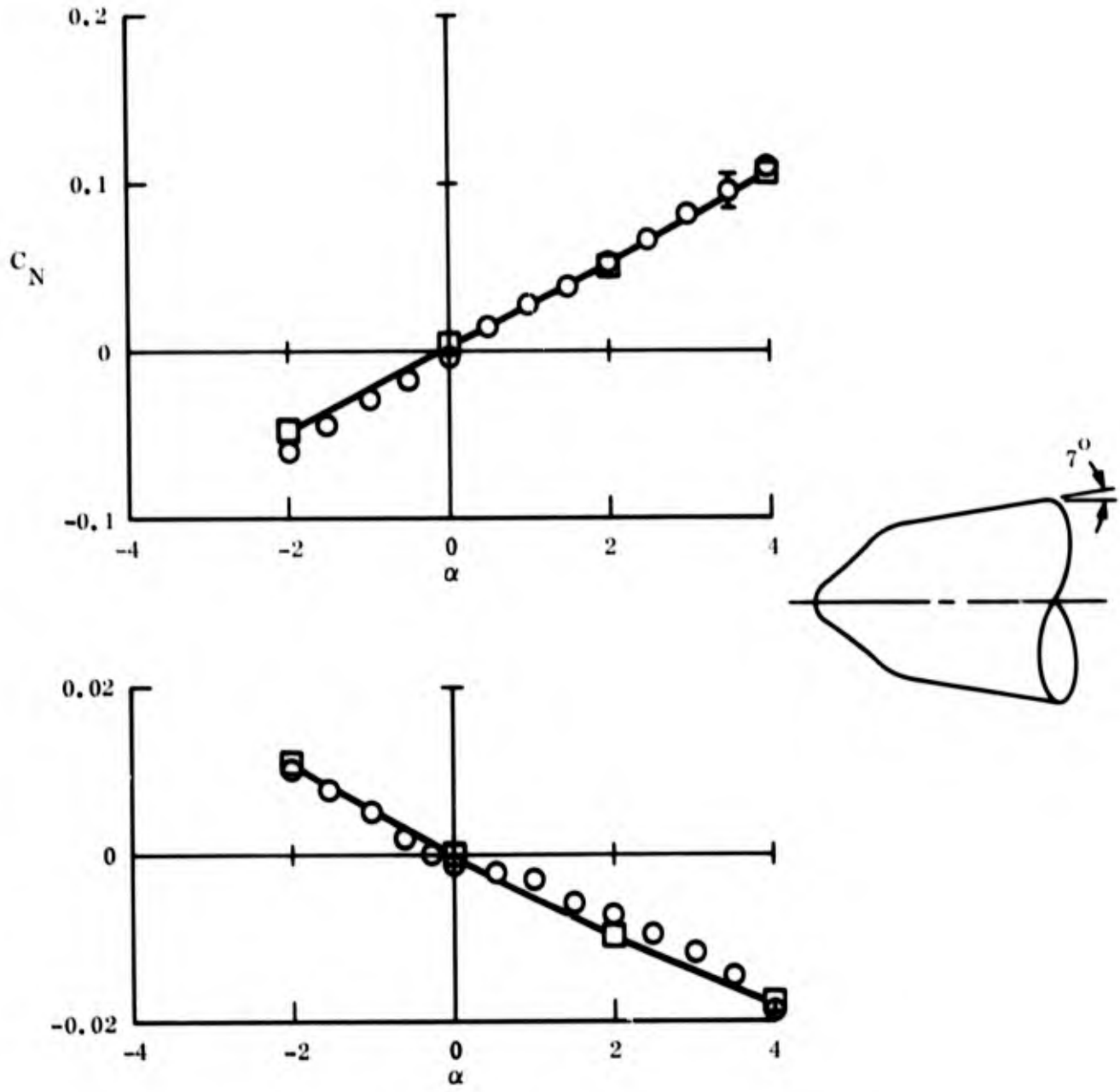

O GROUND TEST DATA, Re_∞ = 22.9 x 10^6/FT

□ 3 DSAP

Xcg/LA = 0.66

θ_c = 7°

Figure 20. Normal Force and Pitching Moment Coefficients for Transitional Asymmetric Shape at M_∞ = 5

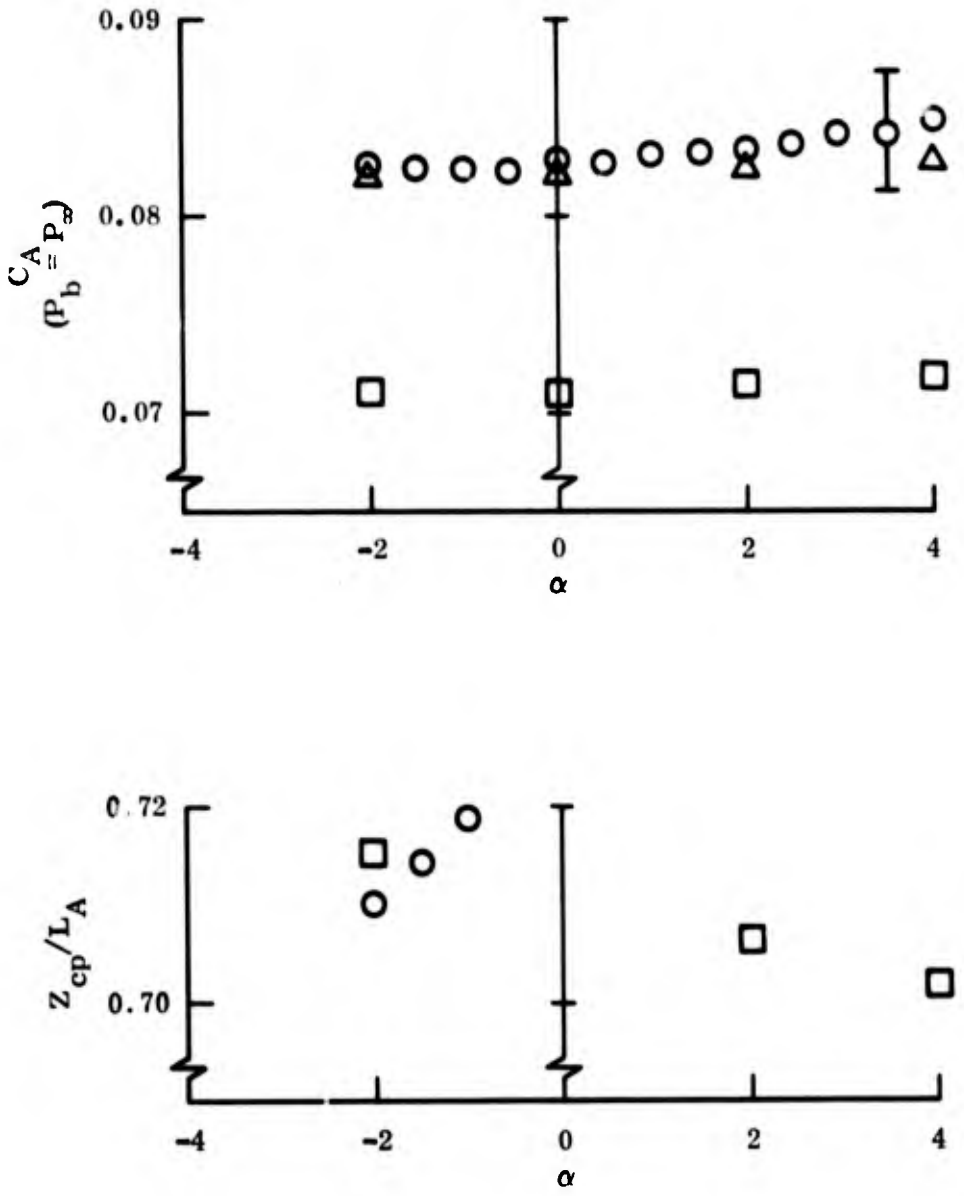

Figure 21. Axial Force Coefficient and Pitch Center of Pressure for Transitional Asymmetric Shape at $M_\infty = 5$

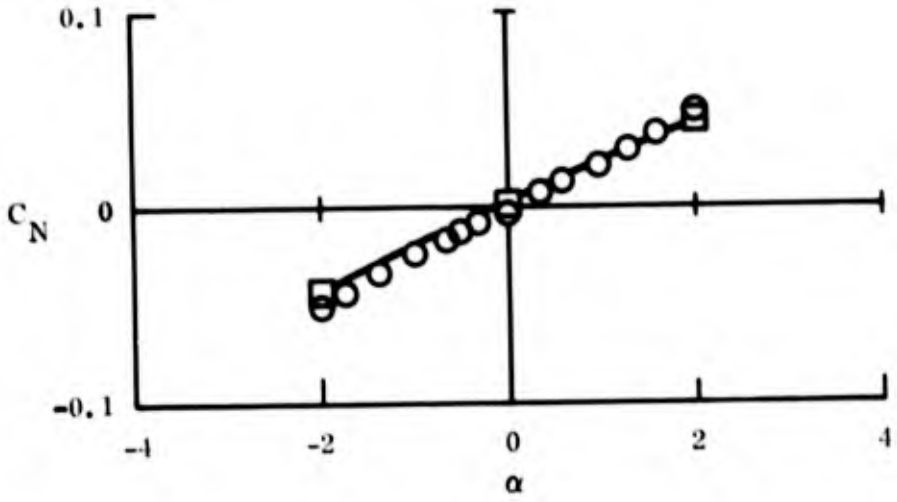

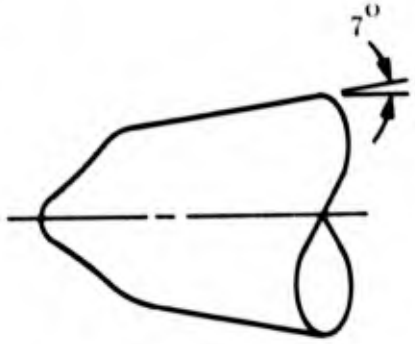

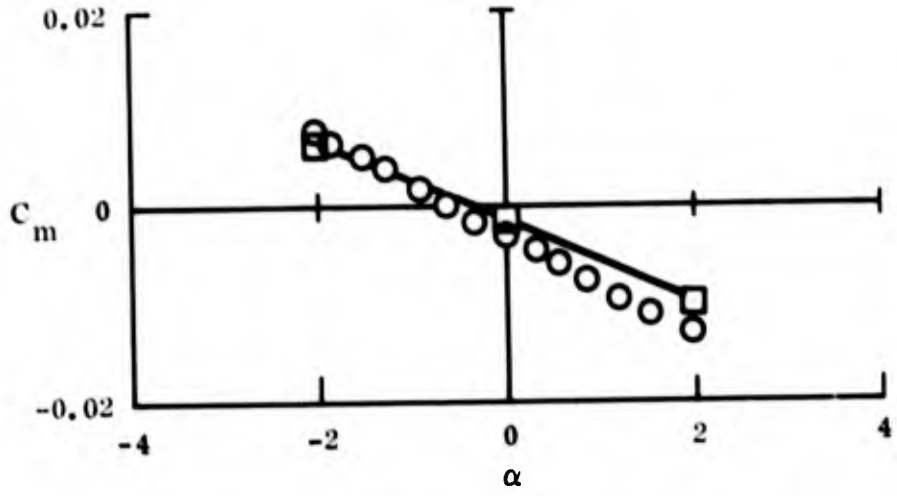

○ GROUND TEST DATA, $Re_\infty = 2.31 \times 10^6/FT$

□ 3 DSAP $Zcg/LA = 0.66$

$\theta_c = 7^\circ$

Figure 22. Normal Force and Pitching Moment Coefficients for Transitional Asymmetric Shape at $M_\infty = 9$

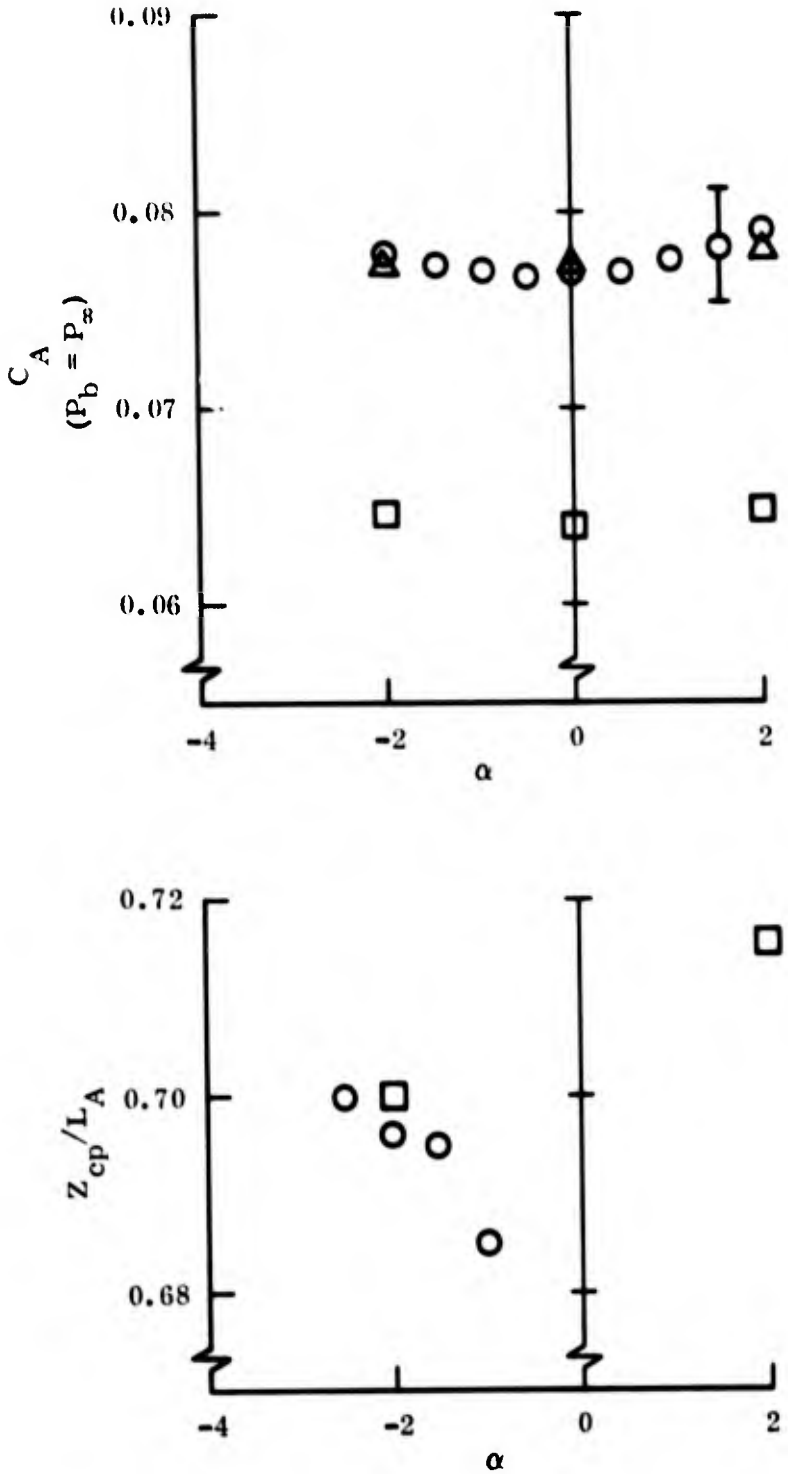

○ GROUND TEST DATA, $Re_\infty = 2.31 \times 10^6$/FT
□ 3DSAP (INVISCID)
△ 3DSAP + TURB. VISCOUS INCREMENT

Figure 23. Axial Force Coefficient and Pitch Center of Pressure for Transitional Asymmetric Shape at $M_\infty = 9$

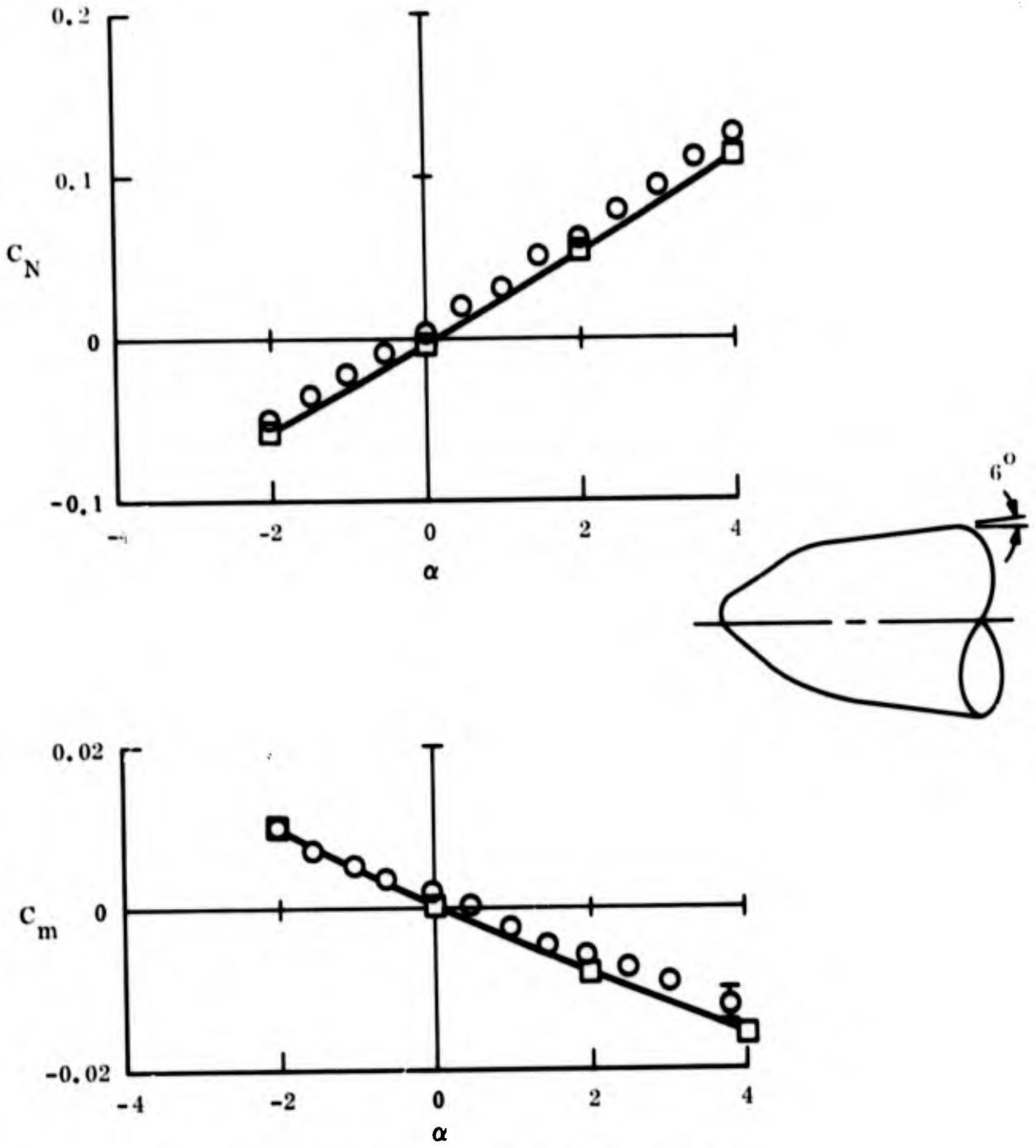

Figure 24. Normal Force and Pitching Moment Coefficients for Turbulent Asymmetric Shape at M_∞ = 5

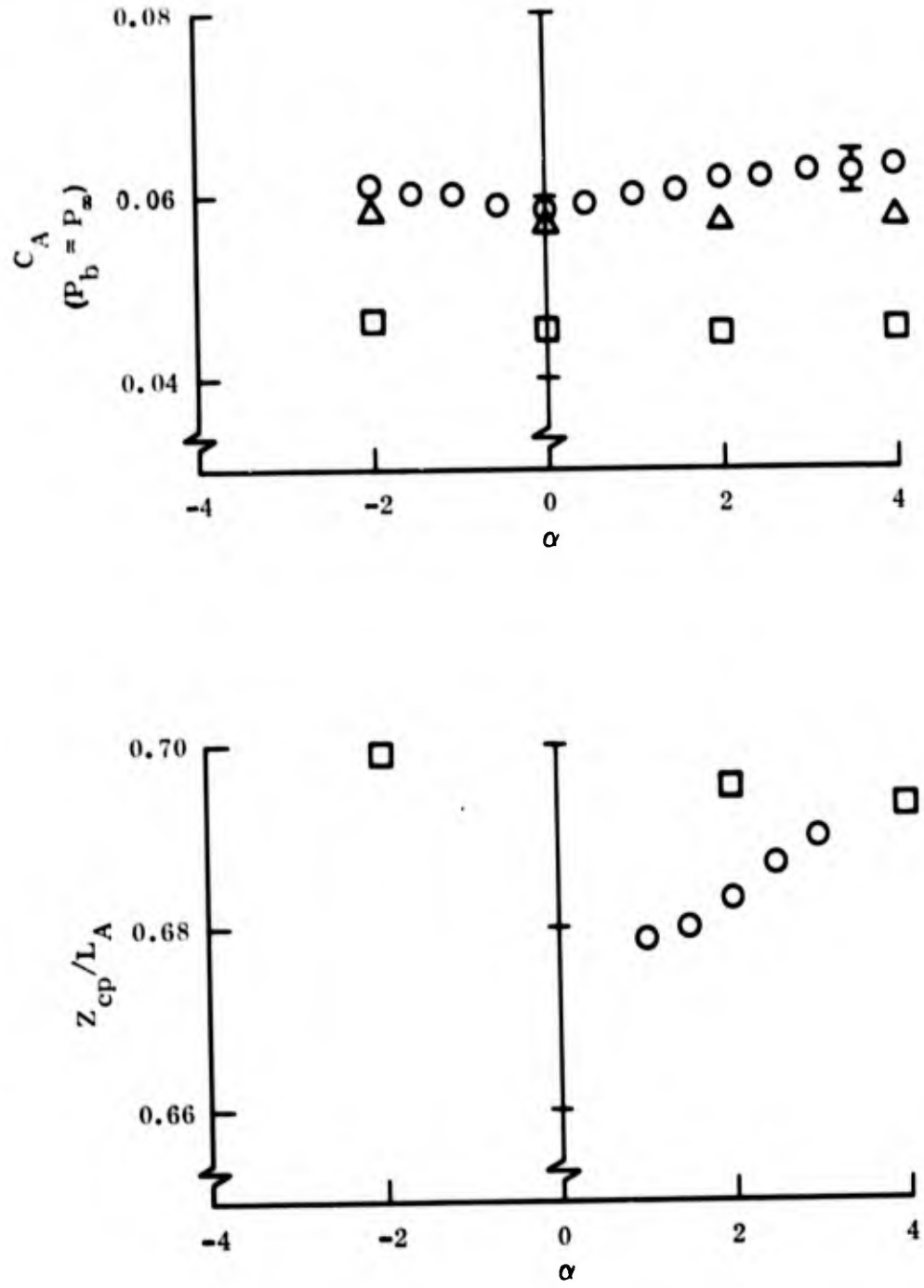

Figure 25. Axial Force Coefficient and Pitch Center of Pressure for Turbulent Asymmetric Shape at $M_\infty = 5$

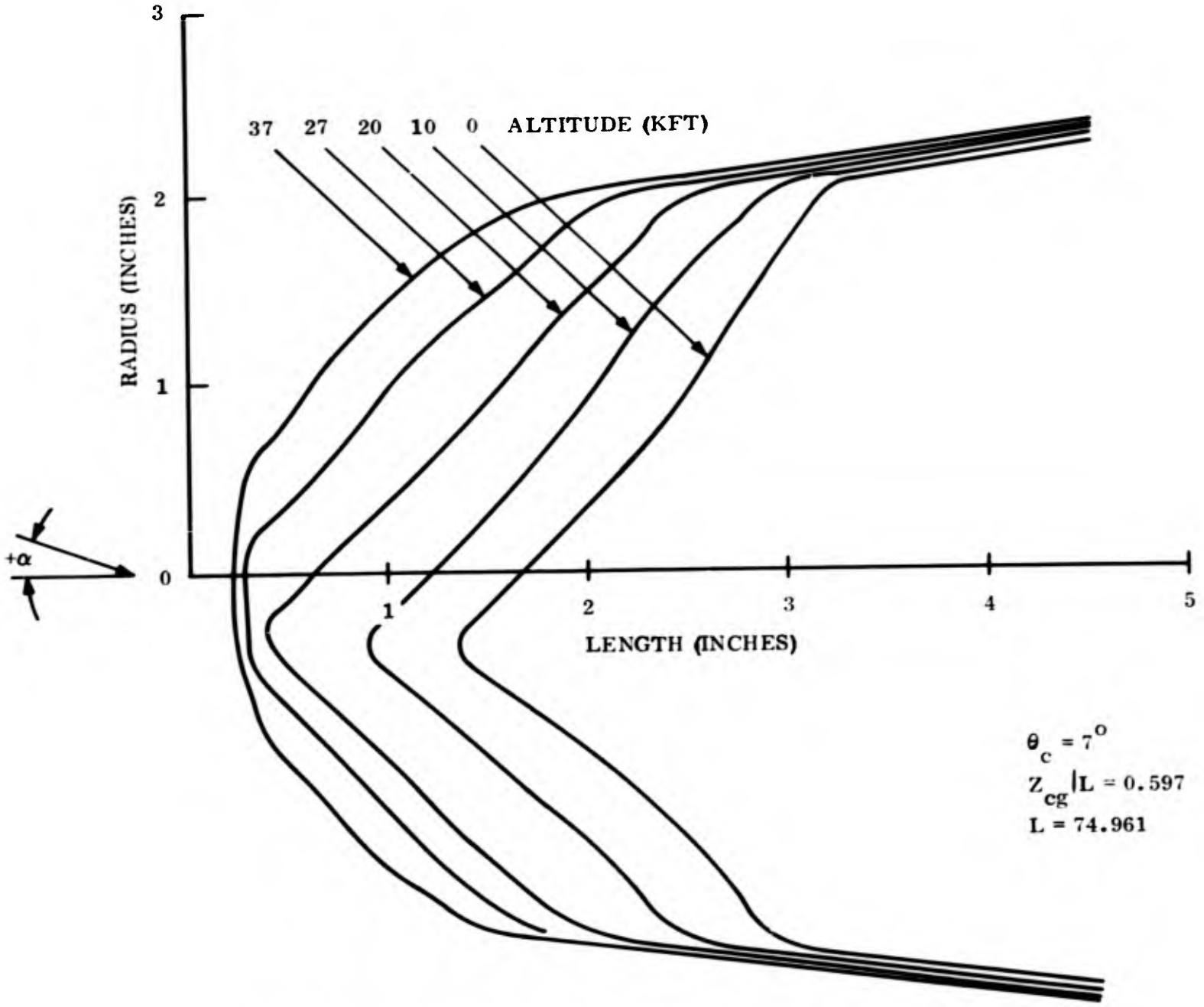

Figure 26. Predicted Nose Shape History for Configuration 16-A (Aerotherm)

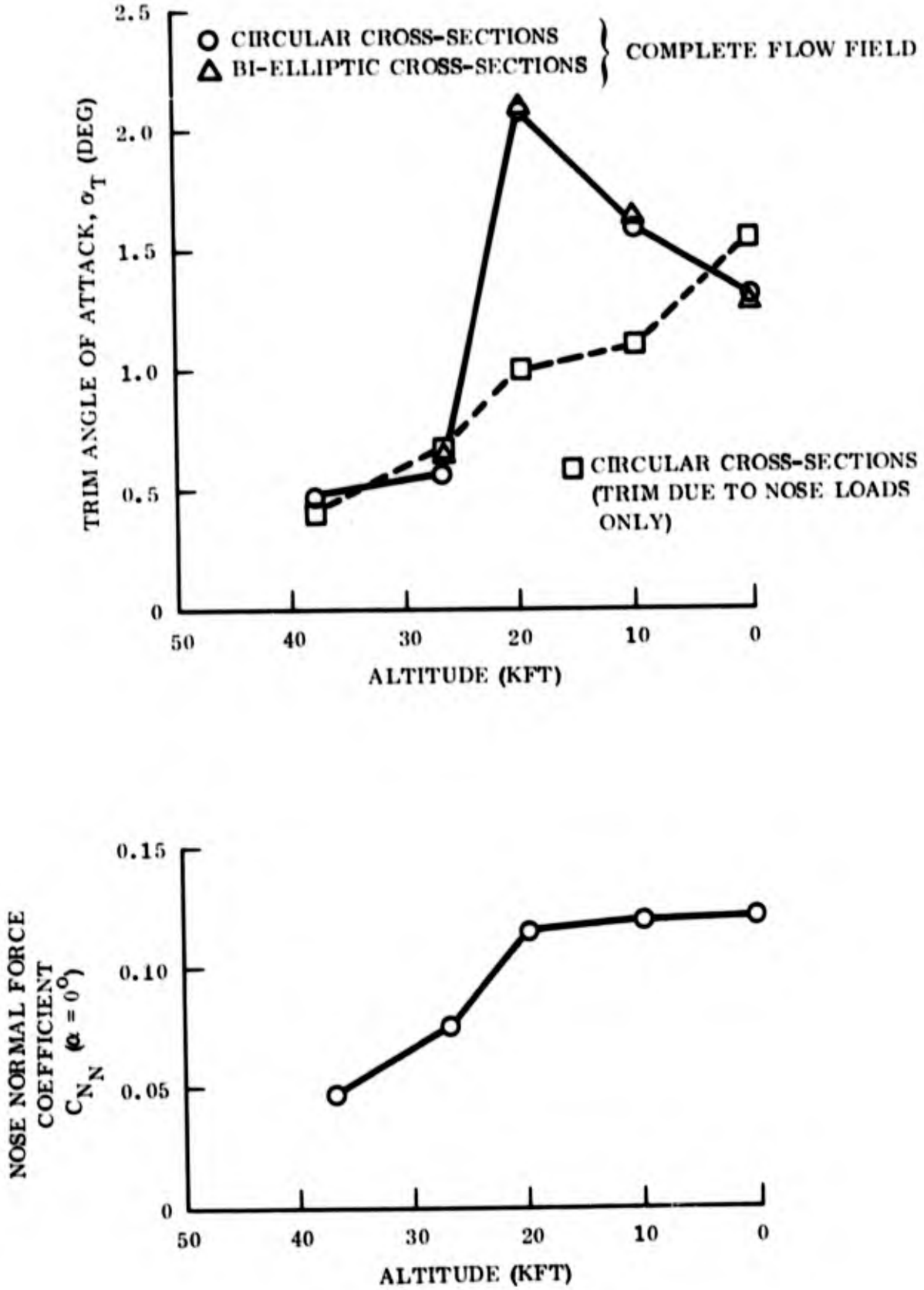

Figure 27. Trim Angle and Nose Load Histories for Configuration 16-A

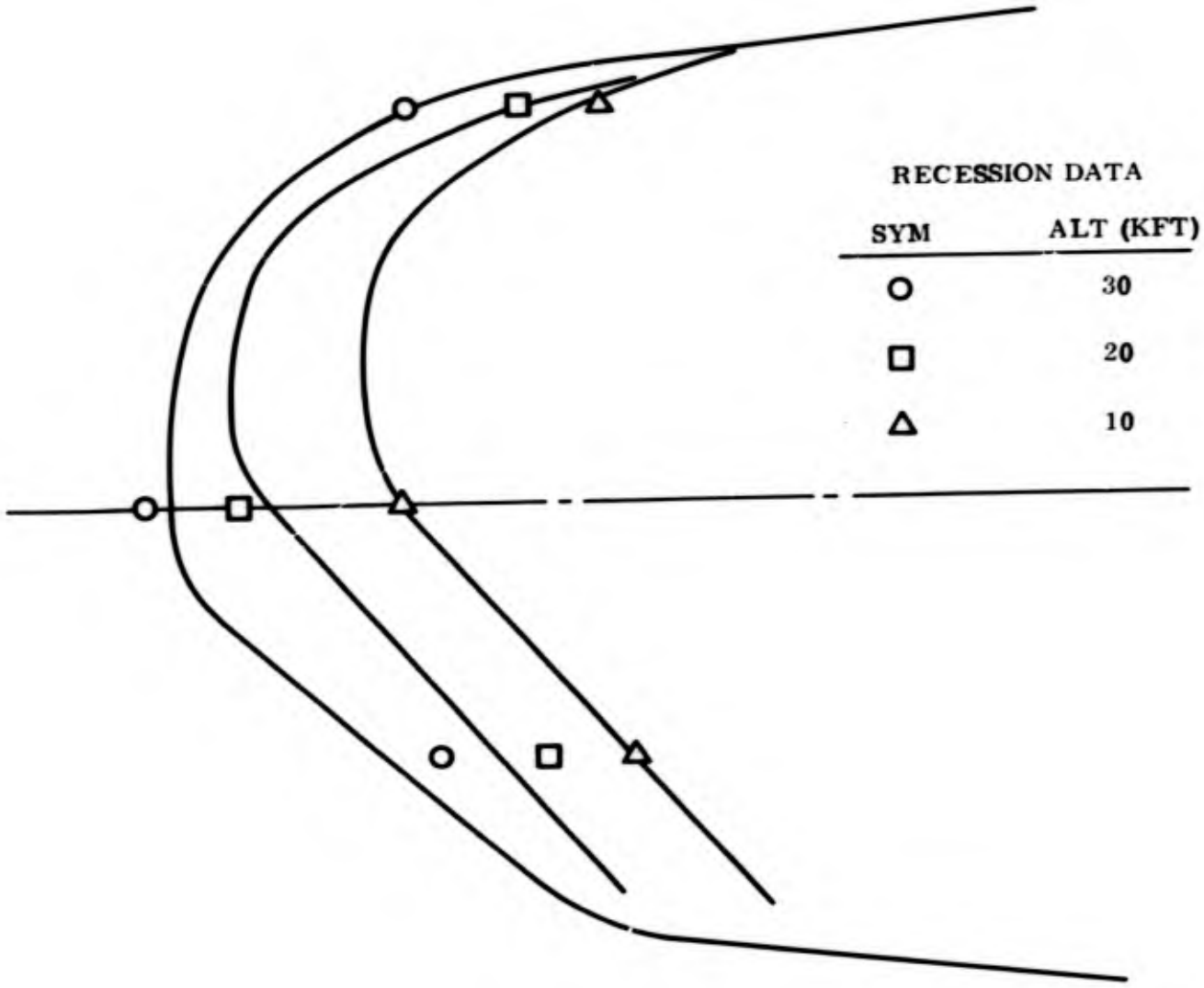

Figure 28. Postulated Nose Shape History

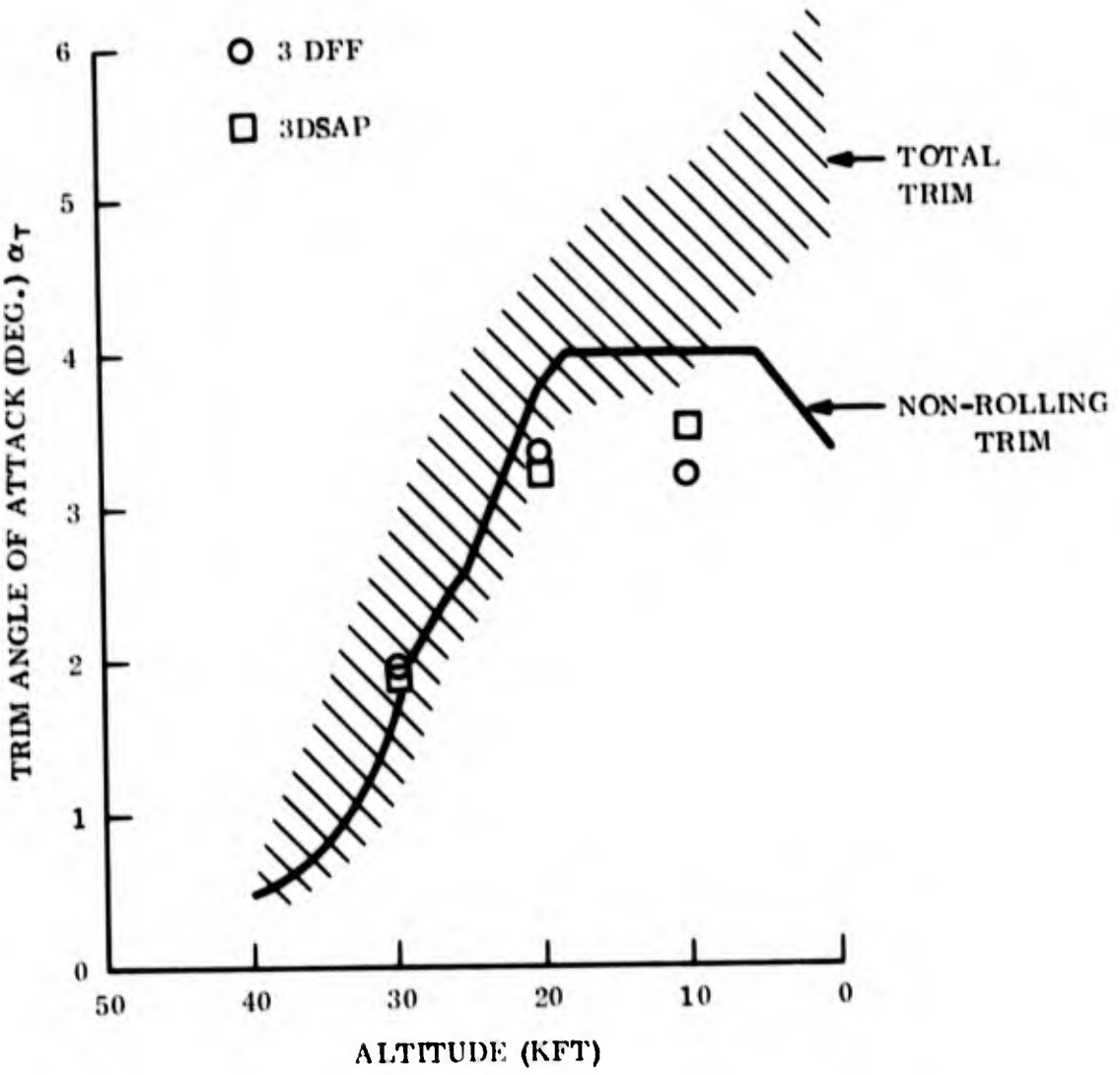

Figure 29. Trim Angle of Attack History

SAMSO/RSSE
P.O. Box 92960
Los Angeles, CA 90009
Attn: Capt. R. Chambers (2 copies)

AFFDL/FXG
Wright-Patterson AFB
Dayton, Ohio 45433
Attn: M. Buck (1 copy)

Defense Nuclear Agency
6801 Telegraph Road
Washington, D. C. 20305
Attn: Lt. Cmdr. R. Nibe

Commander
Naval Surface Weapons Center
White Oak
Silver Springs, Maryland 20910
Attn: S. Hastings (1 copy)

Aerospace Corporation
P.O. Box 92957
Los Angeles, California 90009
Attn: D. Nowlan (2 copies)
T. D. Taylor (1 copy)

Aerotherm Corporation
Division of Acurex Corp.
485 Clyde Ave
MountainView, CA 94040
Attn: C. Nardo (1 copy)

Calspan Corporation
445 Genessee Street
P. O. Box 235
Buffalo, New York 14221
Attn: M. Holden (1 copy)

Effects Technology Inc.
5383 Hollister Avenue
Santa Barbara, CA 93105
Attn: H. King (1 copy)

Physical Sciences Inc.
30 Commerce Way
Woburn, Mass.
Attn: M. Finson (1 copy)

Prototype Development Assoc.
1740 Garry Ave., Suite 201
Santa Ana, CA 929705
Attn: J. Dunn (1 copy)

Science Application Inc.
Valley Forge Executive Mall
Wayne, Pa.
Attn: A. Martellucci

TRW Systems
Defense & Space Systems Group
One Space Park
Redondo Beach, CA 90278
Attn: S. Patay (1 copy)